ENVIRONMENTAL APPLICATIONS OF ESI FT-ICR MASS SPECTROMETRY: THE IDENTIFICATION OF POLAR N, S AND O CONTAINING PAH SPECIES IN CRUDE OIL AND COAL EXTRACTS

Ryan P. Rodgers[2], Geoffrey C. Klein[1], Zhigang Wu[1], and Alan G. Marshall[2]

[1.] Department of Chemistry and Biochemistry, Florida State University, Tallahassee, Florida 32306.
[2.] Ion Cyclotron Resonance Program, National High Magnetic Field Laboratory, Florida State University, 1800 E Paul Dirac Drive, Tallahassee, Florida 32310.

Introduction

The number of distinct chemical components of petroleum is already approaching tens of thousands, and is thus becoming roughly comparable to the number of genes (genome) or proteins (proteome) in a given biological species. Therefore, the inherent complexity of crude oil and its derived products has until now made environmental analysis difficult or in some cases, impossible. Once introduced to the environment, subsequent biotic and abiotic modifications of the petroleum product further complicate an already complex mixture. Traditional analytical techniques such as Liquid Chromatography (LC), Gas Chromatography (GC) and Gas Chromatography – Mass Spectrometry have inadequate chromatographic resolution for the baseline separation of all species present in most petroleum distillates above diesel fuel. As a result, combined techniques (such as GC-MS and LC-MS) are ineffective due to co-eluting species that complicate the mass spectrum and hinder component identification. Furthermore, mass spectrometers commonly employed for GC-MS and LC-MS are low resolution / low mass accuracy quadrupole mass filters or quadrupole ion trap type mass analyzers that are unable to adequately resolve complex mixtures for individual component identification. As a result, the utilization of traditional analytical techniques provides a limited amount of compositional information and is often dominated by a large unresolved "hump", commonly referred to as an unresolved complex mixture (UCM). Fourier Transform Ion Cyclotron Resonance Mass Spectrometry (FT-ICR MS) benefits from ultra-high mass resolving power (greater than one million), high mass accuracy (less than 1 ppm) and rapid analysis which make it an attractive alternative for the analysis of petroleum products that range from crude oil to diesel.

Experimental

Crude Oil Samples. Crude oil and coal samples were prepared by dissolving ~10-20 mg in 3 mL toluene, and then diluting with 17 mL MeOH. Less than 1% (vol/vol) ammonium hydroxide solution (30%) was added to facilitate deprotonation of the acids and neutral nitrogen compounds to yield [M-H]- ions. For positive ion ESI, the MeOH / toluene solution was spiked with HAc to 1% (vol/vol) to facilitate protonation of basic species to yield [M+H]+.

Mass Analysis. The crude oils were analyzed at the National High Magnetic Field Laboratory (NHMFL) with a homebuilt 9.4 Tesla Fourier transform mass spectrometer. Ions were generated externally by a micro-electrospray source and samples delivered by a syringe pump at a rate of 300 nL/min. Approximately 2.2 kV was applied between the capillary needle and ion entrance (heated metal capillary). The externally generated ions were accumulated in a short (15 cm) rf-only octopole for 10-30 s and then transferred via a 200 cm rf-only octopole ion guide to a Penning trap. Ions were excited by frequency-sweep (100-725 kHz @ 150 Hz/μs at an amplitude of 200 Vp-p across a 10-cm diameter open cylindrical cell). The time-domain ICR signal was sampled at 1.28 Msample/s for 3.27 s to yield 4 Mword time-domain data. Ten to two hundred data sets were co-added, zero-filled once, Hanning apodized, and fast Fourier transformed with magnitude computation. Data was collected and processed by a modular ICR data acquisition system (MIDAS).[1,2] Mass spectra were internally calibrated with respect to the most abundant heteroatom containing series over the full mass range. Homologous series were separated and grouped by nominal Kendrick mass and Kendrick mass defect to facilitate rapid identification, as described elsewhere.[3]

Results and Discussion

Sulfur, nitrogen and oxygen containing PAH species are of environmental concern because of their high polarity and subsequently their tendency to migrate from contaminated spill sites. The complexity of polar fractions has hindered individual component identification and largely led to their classification based on compound classes (by way of class based chromatographic separation). The high resolution and mass accuracy afforded by FT-ICR MS allows the identification of individual compound classes (as well as their corresponding type) in mixtures as complex as crude oil, without prior chromatographic separation. Figure 1 shows a broadband positive ESI FT-ICR mass spectrum of South American crude oil with more than 11,000 different species resolved and identified between 300 < m/z < 900 at an average mass resolving power of ~400,000.

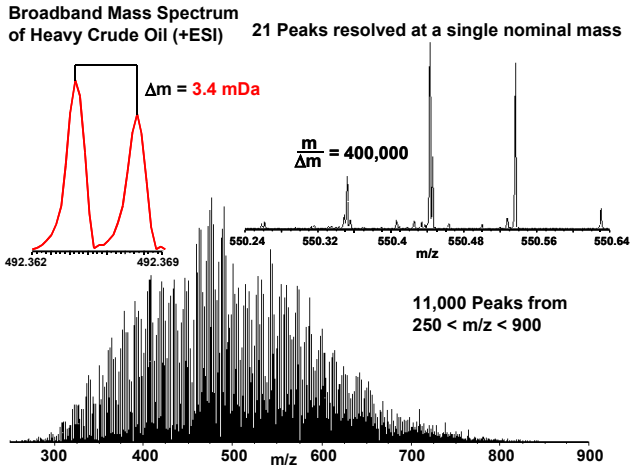

Figure 1. Broadband positive ion ESI FT-ICR mass spectrum of South American heavy crude oil composed of over 11,000 resolved species. A zoom mass inset (top, right) shows 21 peaks resolved at a single nominal mass. A second inset (top, left) shows the baseline resolution of a commonly encountered doublet (SH_4 vs C_3) in petroleum samples.

Similar information is provided from the negative ESI FT-ICR mass spectrum of the same oil. Combined, the two ionization methods allow for the compositional analysis of crude oils at an unprecedented level. Figure 2 shows the combined positive and negative ion ESI FT-ICR mass spectra of the same crude presented in Figure 1 with over 17,000 different species identified. Such detailed analysis provides a powerful tool for the composition based fingerprinting of crude oils for the purpose of contaminant identification. The two ionization methods fundamentally target different compound classes. In positive ion mode, only the basic components of the crude oil are ionized and subsequently detected by the mass spectrometer.

Conversely, in negative mode the acidic species are preferentially ionized and detected.

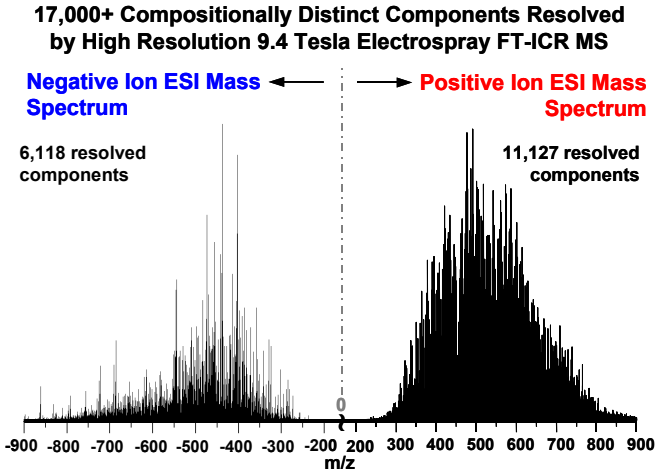

Figure 2. Combined positive (right) and negative (left) ESI FT-ICR mass spectra of a South American heavy crude oil shows over 17,000 resolved species for a single crude oil. Species identified include heteroatom containing crude acids (negative ion) and bases (positive ion) as well as slightly polar nitrogen containing compounds.

Comparisons of crude oils from different geochemical locations allows for a unique composition based fingerprint that can be used for crude oil identification. Figure 3 shows zoom mass insets at a single nominal mass of two crudes collected from different geographical locations. The compositional differences are clearly evident and correlate well with known compositional differences determined by extensive chromatographic class based separations. Similar composition based fingerprinting could conceivably be used to identify a contaminant source even after prolonged weathering. Experiments to test this hypothesis are currently underway and will be presented if completed.

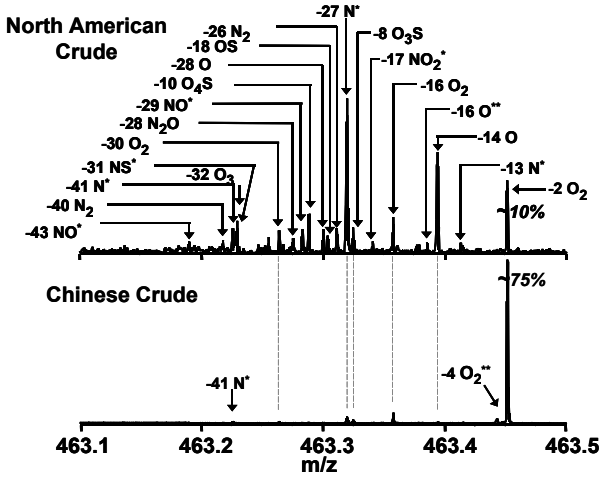

Figure 3. Zoom mass insets for the same single nominal mass of both a North American and Chinese crude oil highlight the differences in composition. The North American crude is much more complex, composed of many different heteroatom containing acidic species. Conversely, the Chinese crude is relatively simple, with carboxylic acid species dominating the majority of the species identified. FT-ICR mass spectral analysis of these two oils confirmed compositional differences discerned in a separate study that employed extensive chromatographic class based separations. The FT-ICR analysis was completed without chromatographic sample pretreatment and in less than one day.

Similar information is also available for coal derived materials. Comparison of crude oil and coal extracts shows that it is quite easy to distinguish on source from another based on the FT-ICR MS compositional analysis. Figure 4 shows the 3-D van Krevelen plots for the shared heteroaromatic classes for both a crude oil and pyridine coal extract.

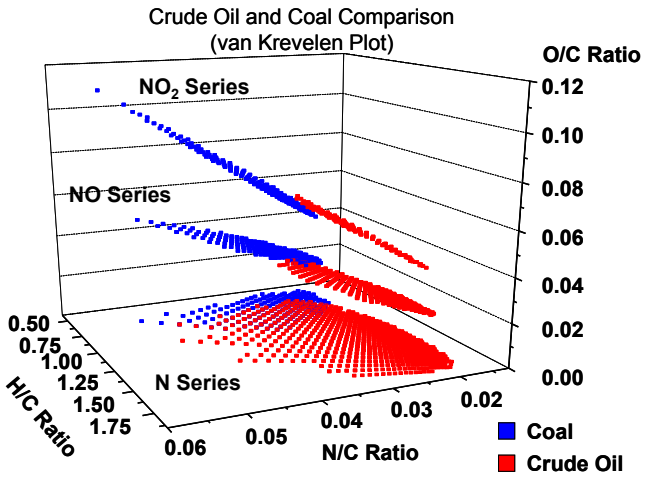

Figure 4. Visualization of the compositional differences is shown in a van Krevelen diagram for both the Coal (in Blue) and Crude Oil (in Red) for a series of shared classes (N, NO, and NO2). The coal classes clearly have a lower H/C ratio (indicative of more aromatic and less alkyl substituted material) than the crude oil asphaltenes allowing for one to be clearly differentiated from the other.

ESI FT-ICR mass spectrometry is a powerful tool for the characterization and identification (at the level of elemental composition for every resolved peak) of both crude oil and coal derived materials. Although its initial application has largely limited to process compositional and bulk characterization analyses, FT-ICR MS stands poised to make a significant impact in environmental applications that entail complex mixture analysis.

Acknowledgment

This work was supported by NSF CHE-99-09502, Florida State University, and the National High Magnetic Field Laboratory in Tallahassee, FL.

References

1. Senko, M. W.; Canterbury, J. D.; Guan, S.; Marshall, A. G. Rapid Commun. Mass. Spectrom., 1996, 10, 1839-1844.
2. Blakney, G. T.; van der Rest, G.; Johnson, J. R.; Freitas, M. A.; Drader, J. J.; Shi, S. D.-H.; Hendrickson, C. L.; Kelleher, N. L.; Marshall, A. G. In 49th ASMS Conference on Mass Spectrom. and Allied Topics: Chicago, IL, 2001.
3. Hsu, C. S.; Qian, K.; Chen, Y. C., *Analytica Chimica Acta,* **1992**, 79-89.

COMBINED USE OF COMPOUND SPECIFIC $\delta^{13}C$ AND δD STABLE ISOTOPE MEASUREMENTS TO AID THE SOURCE APPORTIONMENT OF PAHs

Chenggong Sun, Mick Cooper and Colin E. Snape

Nottingham Fuel & Energy Centre, School of Chemical, Environmental and Mining Engineering (SChEME), University of Nottingham, University Park, Nottingham NG7 2RD, United Kingdom, colin.snape@nottingham.ac.uk

Introduction

The potential of using compound-specific stable carbon isotopic analysis for the source-apportionment of environmental polycyclic aromatic hydrocarbons (PAHs) has been established by O'Malley *et al*. [1,2], Lichtfouse *et al*. [3] and the authors [4-6]. O'Malley *et al*. indicated that PAH arising from wood burning and vehicle emissions exhibited significantly different isotopic signatures [1] and the same authors have also reported the isotopic compositions of *n*-alkanes and PAH produced from combustion of C_3 and C_4 plant species [2]. Lichtfouse *et al*. [3] have reported significant anthropogenic hydrocarbon inputs into soil using a combination of biomarker, $\delta^{13}C$ and ^{14}C analyses. The authors have found that the $^{13}C/^{12}C$ isotopic ratios for PAH derived from coal and wood pyrolysis and diesel particulates vary over a range by *ca*. 8 ‰ which can provide a basis for source apportionment in a number of environments [4-6].

Variations in the carbon stable isotope ratios ($\delta^{13}C$) for PAHs from different sources typically cover a range of only a few ‰, with typically those from coal conversion being close to -24 to -25 ‰, compared to values of -28 to -29 ‰ for transport fuel particulates in the UK. The exception to this relatively narrow range being the exceedingly isotopically light PAHs ($\delta^{13}C$ values as low as –60 ‰) reported by the authors obtained from carbon black production using biogenic methane as the feedstock [7]. To improve the ability of stable isotope measurements to source apportion environmental PAHs, the hydrogen stable isotopes ($\delta^{2}H$) of PAHs from two conversion processes and from petrol and jet fuel particulates have been measured for the first time. The relatively wide range of $\delta^{2}H$ values, in conjunction with the $\delta^{13}C$ values described, potentially provides much greater degree differentiation between PAHs from different sources. We will shortly report on the impact of biodegradation on the $\delta^{2}H$ values for coal-derived PAHs will be addressed.

Experimental

Both compound-specific $\delta^{13}C$ and $\delta^{2}H$ measurements were carried out using a ThermoFinnigan Delta+XP GC-IRMS instrument. The reported carbon isotopic data, expressed in terms of the conventional δ-notation giving the permil (‰) deviation of the isotope ratio from the standard Peedee Belemnite (PDB), represent the arithmetic means of at least two duplicate analyses where variations were generally less than 0.5 ‰. Normal GC-FID and GC-MS analyses were conducted on the aromatics prior to carrying out compound-specific $\delta^{13}C$ measurements. Compound-specific $\delta^{2}H$ analyses were performed using a GC/TC (High Temperature Conversion; 1450°C) unit, interfaced to the mass spectrometer [8,9]. Reported deuterium measurements are expressed as the permil deviation of the isotope ratio from Vienna Standard Mean Ocean Water (VSMOW). Data reported are the arithmetic means of at least two duplicate analyses, where variations were generally less than 3 ‰.

Figure 1 illustrates a typical chromatogram obtained from GC-TC-IRMS analysis.

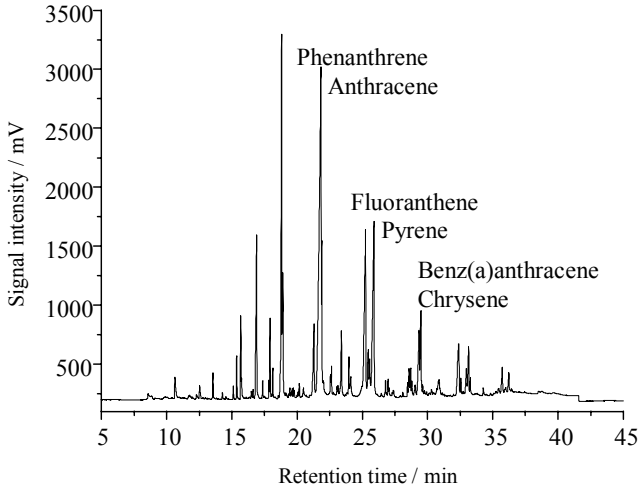

Figure 1 Chromatogram obtained from GC-TC-IRMS analysis of the Gasworks coal tar

Results and Discussion

Table 1 lists the carbon isotopic ratios of PAHs extracted from the high temperature carbonization and gas works (former Town gas plants in the UK) coal tars and the jet fuel and gasoline particulates. As expected from our earlier work, most of the PAHs have stable carbon isotopic ratios in the range of –22 to –30 ‰. Since British UK bituminous coals have bulk isotopic values close to –23 ‰, it may be concluded that, when PAHs are released as primary devolatisation products with minimal structural alteration, little in the way of isotopic fractionation occurs. However, when PAHs result from ring-growth, the smaller hydrocarbons in the primary volatiles undergo a series of complex transformations involving carbon-carbon bond formation, cyclisation and/or ring fusion. In one, or all of these processes, ^{12}C will be preferentially incorporated into the PAH where a kinetic isotope effect is operative. This could be the case for the coal tar from the Town gas plant having $\delta^{13}C$ values ranging from –27.5 to-29.5 ‰[5].

Typical carbon isotopic values of UK transport fuels have been found to be in the range –27 to –29 ‰. Again, PAHs derived from these sources reflect the carbon isotopic signature of the parent fuels to some extent (Table 1). The gasoline-derived PAHs display a trend to isotopically lighter values with increasing molecular mass. In contrast, the jet fuel-derived PAHs are isotopically heavier but display the same trend to isotopically lighter values with increasing molecular mass as for the petrol. Although detailed studies are required to understand these isotopic trends, the data in table 1 indicated that corresponding PAHs differ in isotopic composition by 2-4 ‰ for petrol and jet fuel particulates.

Li *et al*. [13] have determined $\delta^{2}H$ composition of individual alkanes in crude oils from the Western Canadian Sedimentary Basin, as a means of characterization of source organic matter, thermal maturity and migration. Comparison of individual alkanes from oils sourced from different geological provinces revealed a large range of $\delta^{2}H$ values, often of the order of *ca* 100 ‰, in addition to variations between alkanes in the same sample of *ca* 30 ‰. Also of relevance

are the δ^2H values in the range of –80 to –100 ‰ for a number of bituminous coals reported by Mastalerz et al.[11].

Table 1 $\delta^{13}C$ values for PAHs from selected coal tars and transport fuel particulates

PAH	Gasworks coal tar	HT coal tar	Jet fuel	Gasoline
Phenanthrene	-27.5	-24.8	-22.7	-26.5
Anthracene	-27.5	-24.8	-22.7	-26.5
Fluoranthene	-28.5	-24.5	-23.5	-27.1
Pyrene	-28.3	-24.5	-23.2	-26.9
Benz(a)anthracene	-28.9	-24.2	-24.1	-27
Chrysene	-28.9	-24.2	-23.5	-27
Benzo(b)fluoranthene	-28.8	-24.8	-25.7	-27.8
Benzo(k)fluoranthene	-28.8	-24.8	-25.7	-27.8
Benzo(a)pyrene	-28.9	-25.2	-25.5	-28.5
Indeno(1,2,3-cd)pyrene	-29.5	-26.4	-27.8	-29.4
Dibenz(a,h)anthracene	-29.5	-26.4	-27.8	-29.4
Benzo(ghi)perylene	-30	-26.6	-28.1	-29.6

Table 2 listed the δ^2H isotopic signatures for the PAHs derived from the samples investigated here. Of note are the large differences in $^2H/^1H$ isotopic ratio, both between samples derived from the different sources, where differences of *ca* 40‰ are observed, and between PAHs in the same sample, where variations of up to 20‰ are apparent. The jet fuel PAHs are isotopically lighter than those from petrol. Likewise, PAHs from high temperature carbonization are lighter and more nearer the isotopic values of whole coals than those in the gasworks tar. Figure 2 illustrates the correlation between δ^2H and $\delta^{13}C$ isotopic signatures of PAHs in the range phenanthrene to chrysene, indicating the very clear differentiation between the four samplesinvestigated. Thus, the advantages for source apportionment of utilizing both $\delta^{13}C$ and δ^2H isotopic values become readily apparent.

Table 2 δ^2H values for PAHs from selected coal tars and transport fuel particulates

PAH	Gasworks coal tar	HT coal tar	Jet fuel	Gasoline
Phenanthrene	-49.3	-73.2	-	-61.5
Anthracene	-49.3	-	-	-61.5
Fluoranthene	-42.2	-67.9	-74.3	-49.1
Pyrene	-40.0	-65.3	-74.1	-54.7
Benz(a)anthracene	-38.7	-72.1	-71.1	-47.1
Chrysene	-33.5	-72.6	-71.1	-47.1
Benzo(b)fluoranthene	-33.5	-81.1	-61.2	-47.0
Benzo(k)fluoranthene	-34.0	-81.1	-61.2	-47.0
Benzo(a)pyrene	-33.2	-68.3	-60.2	-51.2
Indeno(1,2,3-cd)pyrene	-33.2	-75.5	-68.9	-49.2
Dibenz(a,h)anthracene	-33.2	-	-68.9	-51.2
Benzo(ghi)perylene	-32.2	-71.6	-67.5	-54.0

Conclusions

Variations in the carbon stable isotope ratios ($\delta^{13}C$) for PAHs from different sources cover a range of only a few ‰, with typically

To improve the ability of stable isotope measurements to source apportion environmental PAHs, the hydrogen stable isotopes of PAHs reported here have demonstrated the wide range of δ^2H values that exists. These have been used in conjunction with the $\delta^{13}C$ values to provide a much greater degree of differentiation between petrol and jet fuel-derived PAHs and between PAHs from different coal conversion processes than the $\delta^{13}C$ values alone.

Acknowledgement. The authors thank the European Coal & Steel Community (ECSC) for financial support and Prof. David Lee, Manchester Metropolitan University and Prof. Chris Wilson, Sheffield University with Qinetiq for providing the jet fuel particulate sample.

References

(1) O'Malley, V.P.; Abrajano Jr., T.A.; Hellou, J. *Org. Geochem.*, **1994**, *21*, 809-822.
(2) O'Malley, V.P., Burke, R.A.; Schlotzhauer, W.S. *Org. Geochem.*, **1997**, *27*, 567-581.
(3) Lichtfouse, E.; Budzinski, H.; Garringues, P.; Eglinton, T.I. *Org. Geochem.* **1997**, *26*, 353-359.
(4) McRae, C.; Love, G.D.; Murray, I.P.; Snape, C.E.; Fallick, A.E. *Anal. Commun.* **1996,** *33*, 331-333.
(5) McRae, C.; Snape, C.E.; Fallick, A.E. *Analyst*, **1998**, *123*, 1519-1523.
(6) McRae, C.; Sun, C-G; Snape, C.E.; Fallick, A.E.; Taylor, D. *Org. Geochem.* **1999**, *30*, 881-889.
(7) McRae, C.; Sun, C-G; Snape, C.E.; Fabbri, D; Tatari, D.; Trombini, C.; Fallick, A.E. *Environ. Sci. & Technol.,* 2000, **34**, 4684-4686.
(8) Burgoyne T. & Hayes J.M. *Anal. Chem*. **1998**, *70*, 5136.
(9) Hilkert A.W.; Douthitt C.B.; Schlü er H.J.; Brand W.A. *Rapid Comm. Mass. Spec*., **1999**, *13*, 1226-1230.
(10) Li M.; Huang Y.; Obermajer M.,;Jiang C.; Snowdon L.R. & Fowler M.G. *Org. Geochem*. **2001**, *32*, 1387-1399.
(11) Mastalerz M. & Schimmelmann A. *Org. Geochem*. **2002**, *33*, 921-931.

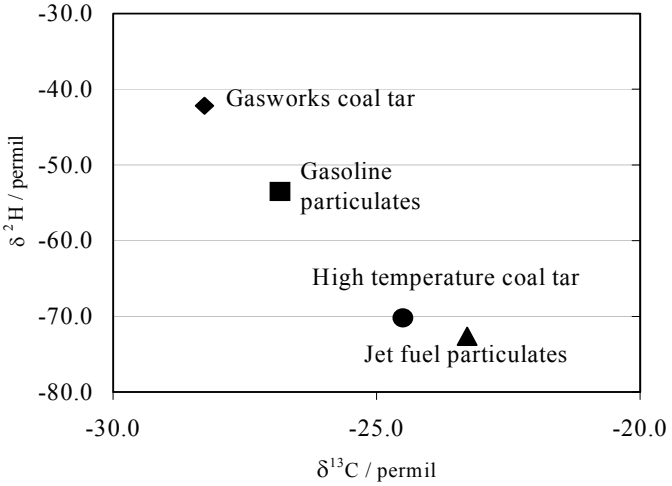

Figure 2 Correlation of $\delta^{13}C$ and δ^2H for selected PAHs generated by transport fuels and coal utilisation

NANOSTRUCTURE EFFECTS UPON SOOT OXIDATION

Randy L. Vander Wal and Aaron J. Tomasek
NCMR c/o NASA-Glenn
M.S. 110-3
21000 Brookpark Rd.
Cleveland, OH 44135

Introduction

Studies of soot oxidation have ranged from *in situ* flame studies to shock tubes to flow reactors [1]. Each of these systems possesses particular advantages and limitations related to temperature, time and chemical environments. Despite the aforementioned differences, these soot oxidation investigations share three striking features. First and foremost is the wide variation in the rates of oxidation. Reported oxidation rates vary by factors of +6 to - 20 [2] relative to the Nagle Strickland-Constable (NSC) rate for graphite oxidation [3]. Rate variations are not surprising, as the temperatures, residence times, types of oxidants and methods of oxidation differ from study to study. Nevertheless, a valid explanation for rate differences of this magnitude has yet to be presented.

Experimental

Soots possessing different nanostructures were produced by pyrolysis of acetylene, benzene or ethanol. These soots still in aerosol form were introduced into the post flame gases produced by a lean, premixed flame supported on a sintered metal burner. The soot and a portion of the post combustion gases were directed into a 1 inch outer diameter quartz chimney of 6 inches in length, placed directly above the quartz tube. With this setup, the temperature along the chimney axis was 750 +/- 30 ºC, as measured by a type K thermocouple. This variation was within the error range of the thermocouple, +/- 25 ºC, and hence it was taken as constant at 750 ºC. With a known entrance gas velocity, the residence time of the soot within the chimney is readily calculated based on buoyant acceleration as 75 +/- 5 ms.

With this configuration, oxidation was conducted well above the flame front, in the post flame gases. Burning with equivalence ratio less than one ensures that that the OH concentration within the post-flame gases is insignificant [10]. Given vastly slower rates for oxidation of carbons by H_2O or CO_2, the primary oxidant was considered to be the excess O_2 [1]. The soot stream appeared as a thin cylinder with yellow C_2 swan band emission associated with burning soot. Partially oxidized soot was collected at the chimney exit by thermophoretic sampling directly upon a lacey TEM grid.

Results and Discussion

Figure 1 plots the mass burnout rates versus free O_2 concentration for the soots derived from the different fuels. Burnout rates are calculated relative to the initial particle size before introduction into the flame environment. The mass loss rate increases with increasing O_2 concentration as expected for all soots, yet the soots derived from benzene and acetylene exhibit a dramatic difference in their oxidation rates. As observed, the acetylene soot requires a much higher ambient O_2 concentration to achieve the same level of burnout (for any given reaction duration) as the benzene derived soot. The soot derived from ethanol exhibits a very similar rate as the benzene soot. The faster burnout rate for the benzene and ethanol derived soots is also reflected in their complete oxidation at O_2 concentrations far lower than that of the acetylene derived soot, despite similarly sized primary particles for these two soots. Plotted for reference is the calculated NSC rate at each O_2 concentration at the measured post-flame gas temperature [3]. As seen in Fig. 1, the measured rates for the graphitic acetylene soot lie much closer to the NSC rates. Notably the oxidation rates of all the soots exceed the NSC rate. HRTEM images of the soot have been obtained and reported elsewhere [4]. These images form the basis for our subsequent discussion and lattice fringe analysis as follows next.

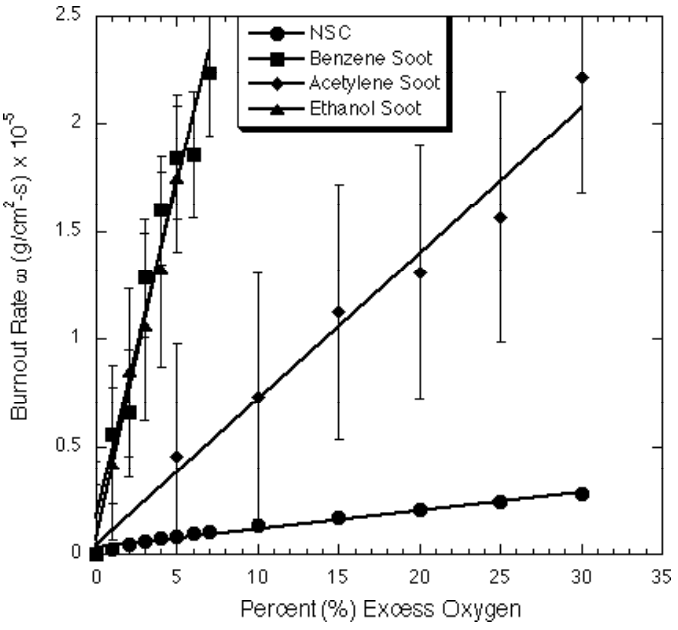

Figure 2 Dependence of soot mass burnout rate with O_2 percentage in the post-flame gases. The NSC rate is also shown for comparison.

Soot Structure. Although the relation between carbon structure and reactivity is well-known in carbon science from thermal and oxidative studies of and graphite [5]; the relation for soot remains unstudied. It is well-known that graphite oxidation proceeds anisotropically, i.e, the reactivity of basal plane carbon atoms is far lower than that of edge site carbon atoms. Measurements by Rosner and Allendorf observed a 10 - 100-fold reactivity difference between isotropic and pyrolytic graphite, intrepreted on the basis of the differerent reactivities of carbon atoms within basal plane versus edge site positions [5].

Consequently, the observed reactivity will be an average of basal versus edge site carbon atom reactivities for graphitic layer planes of finite dimensions [3]. As the layer plane size decreases, the number of edge site carbon atoms will necessarily increase in proportion to the number of basal plane carbon atoms, allowing one to expect the overall reactivity to increase. In addition to the size of the graphene segments, their relative curvature will also impact their oxidation rate. Curvature arises from 5-membered rings within the aromatic framework [6]. This curvature imposes bond strain because the orbital overlap giving rise to the electronic resonance stabilization is lessened [7]. Therein the C-C bonds are weakened and individual atoms are more exposed, i.e. they are more susceptible to oxidative attack. It is for these same reasons that fullerenes and carbon nanotubes are less resistant towards oxidation than planar graphite [7, 8].

This duality of reactive sites forms the physical basis for the NSC oxidation rate expression which takes into account both edge and basal plane carbon sites and their associated reactivities [3]. However, this semi-empirical rate is based on pyrolytic graphite, a

structure with extended basal planes and correspondingly few edge site carbon atoms. Consequently the overall oxidation rate would be expected to be relatively low compared to most other carbons possessing a less graphitic structure. Notably there is no corresponding model or rate expression that takes into account the curvature of graphitic layer planes and the associated impact upon oxidative stability.

Thus the reactivity of a soot particle towards oxidation depends upon its nanostructure, i.e. the size, orientation and organization of the graphene layer planes. Variations in the graphene layer plane dimensions, curvature, and relative orientation will greatly impact the reactivity of the individual graphene segments, and hence the overall particle reactivity. Yet as discussed, little attention has been given to soot particle nanostructure and its impact upon reactivity towards oxidation within combustion systems. To the degree to which the soot nanostructure reflects a dependence upon inception and growth conditions, so too will its oxidation rate reflect a similar dependence. Our results clearly illustrate a dependence of the burnout rate upon the soot nanostructure as governed here by both the initial fuel and soot growth conditions.

Conclusions

The work reported here illustrates a dependence of the soot particle nanostructure upon synthesis conditions; namely temperature, time and initial fuel identity. Such structural variations in the graphene layer plane dimensions necessarily alters the ratio of basal plane versus edge site carbon atoms. A corresponding variation in the overall reactivity, reflecting an average of the different reactivities associated with these specific atomic sites arises. This variation is illustrated here between a disordered soot derived from benzene and a graphitic soot derived from acetylene. Their oxidation rates differ by nearly 5-fold. Curvature of layer planes, as observed for an ethanol derived soot, is found to substantially increase oxidative reactivity. Relative to fringe length as a manifestation of graphitic structure, curvature more effectively increases reactivity towards oxidation. Larger variations in oxidation behavior may be expected, depending upon the soot synthesis conditions. Other physical properties may similarly be affected.

Acknowledgements. This work was supported by a NASA NRA 99-HEDs-01 combustion award (RVW) administered through NASA cooperative agreement NAC3-975 with The National Center for Microgravity Research on Fluids and Combustion (NCMR) at The NASA-Glenn Research Center. The authors gratefully acknowledge Gordon M. Berger for assistance with the experiments and Dr. Y. L. Chen and David R. Hull for the TEM imaging.

References

(1) Kennedy, I. M.; *Prog. Energy Combust. Sci.* **1997,** *23 ,* 95. (and references therein).
(2) Puri, R.; Santoro, R. J.; and Smyth, K. C.; *Combust. and Flame* **1994,** *97,* 125.
(3) Nagle, J. Strickland-Constable, R. F.; *Proc. of the Fifth Carbon Conf.* **1962,** *1,* pp.154-162.
(4) Vander Wal, R. L.; and Tomasek, A. J.; *Combust. and Flame* (in press).
(5) Rosner, D. E.; and Allendorf, H. D.; *AIAA Journal* **1968,** *6,* 650.
(6) Kroto, H. W.; Heath, J. R.; O'Brien, S. C.; Curl, R. F.; and Smalley, R. E.; *Nature*, **1985,** *318,* 162.
(7) Dresselhaus, M. S.; Dresselhaus, G.; and Eklund, P. C.; *Science of Fullerenes and Carbon Nanotubes,* Academic Press Inc. **1996**.
(8) "*Carbon Nanotubes, Preparation and Properties*", CRC Press Inc., (T. W. Ebbesen Ed.), **1997**.

CURRENT STATUS AND FUTURE TREND OF NITROGEN OXIDES EMISSIONS IN CHINA

Hezhong Tian, and Jiming Hao

Air Pollution Control Division
Dept. of Environ. Sci. & Eng.
Tsinghua University
Tsinghua Campus, Haidian District
Beijing, 100084, P.R. China

Introduction

In recent years, NO_X emissions produced by energy use and economic activities in China have received increasing attention from Chinese government as well as from domestic and foreign scientists, because of its implication in the chemical complexity of acid rain, photo-chemical smog and fine particulate (PM_{10}/$PM_{2.5}$) formation in air which causes a threat to human health and ecosystem. Therefore, knowing about the present status and future trend of NO_X emissions in China will play an active role in regulating NO_X control strategies.

In this study, the database of historical energy consumption in China was established, as well as the database of future energy demand between 2000 and 2030, which was deduced from energy consumption in 2000 by the means of sectoral analysis methodology. The database of NO_X emission factors specified by different economic sectors and different fuel types was constituted on the basis of field experiments and reference survey. Then, the present and future NO_X emissions in China were evaluated and analyzed.

Scope and Methodology

Scope. The regions studied cover 31 provinces/autonomous regions/municipalities on the Chinese mainland. Eight large economic sectors are taken into consideration, including thermal power generation (POW), other energy transformation (OTR), agriculture (AGR), industry (IND), transportation (TRA), construction (CON), service (SER), and residential consumption (RES). Eleven types of fossil fuels are investigated, i.e., coal, coke, crude oil, gasoline, kerosene, diesel, residual oil, LPG, refinery gas, coal gas, natural gas, and other gases [1].

The necessary energy consumption data during the period from 1980 to 2000 were derived from energy balance tables of the whole nation and/or each province in terms of economic sectors, fuel types, and provinces. While, the energy demand up to 2030 were projected by the means of sectoral analysis methodology, which were based on the relevant statistical data in China Statistical Yearbook [2,3].

Methodology. Emissions of NO_X in China was evaluated by combining energy consumption and NO_X emission factors, which can be expressed by the following hierarchical formula [1,4]:

$$Q_T^N(t) = \sum_i Q_i^N(t) \quad (1)$$

$$Q_i^N(t) = \sum_j Q_{i,j}^N(t) \quad (2)$$

$$Q_{i,j}^N(t) = \sum_f \sum_k Q_{i,j(k),f}^N(t) \quad (3)$$

$$Q_{i,j(k),f}^N(t) = (1 - P_{i,j(k),f}^N(t)) K_{i,j(k),f}^N(t) F_{i,j(k),f}(t) \times 10^{-3} \quad (4)$$

Where: Q^N=Emissions of NO_X calculated as NO_2; K^N=Emission factor of NO_X weighted as NO_2; F=Fuel consumption; P^N=Efficiency of NO_X removed by pollution control measures; T=China; t=Year; i=Province; j=Economic sector; f=Fuel type; $j(k)$=Emission source category in the economic sector j.

Emission factors of NO_X. The database of NO_X emission factors was constituted based on field experiments and literature investigation, which was specified by different economic sectors and different fuel types.

Results and Discussion

Economic growth and energy consumption. Since 1980s, China's economy has been growing rapidly. The national GDP grew from 451.78 billion Yuan in 1980 to 8944.22 billion Yuan in 2000, with an annual average growth rate of 9.7%(**Figure 1**). It also can be seen that the structure of the economy and the share of different economic sectors have changed gradually through years of economic and product restructuring. While the Secondary Industry (including industry and construction) still keeps a fairly steady share of total GDP, the Tertiary Industry, which is less energy–intensive, has gradually expanded to approximately one-third of the total GDP.

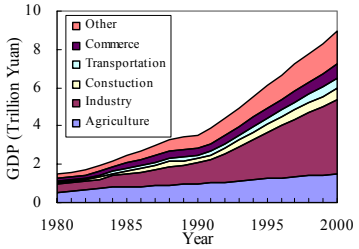

Figure 1. The structure of China's national GDP, 1980~2000.

In the same time, the total primary energy consumption has increased from 602.75Mtce to 1302.97Mtce (**Figure 2**). With the continuously rapid growth of economy, China's energy consumption experienced a steadily increase until 1996, at which primary energy consumption reached a peak value of 1389.48Mtce. However, a decline in primary energy use has occurred in the late 1990s. Contrary to all earlier expectations, the years between 1996 and 2000 witnessed a continuous decline in China's consumption of primary energy, mostly driven by the reduced use of coal--the most significant fossil fuel energy in China. From a peak value of 1447Mt in 1996, China's coal use dropped to 1245Mt in 2000, and coal's share of total primary energy consumption fell from 74.7% to 66.1%.

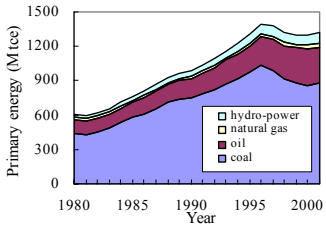

Figure 2. The primary energy consumption in China, 1980~2000.

Current status of NO_X emissions in China. Based on national and provincial energy consumption data and specific NO_X emission factors, the national gross NO_X emissions in the period of 1980 to 2000 are evaluated (see **Figure 3**). As can be seen, with the continuously rapid growth of economic activity and coal-dominated energy consumption, total emissions of NO_X in China grew steadily in the past two decades, from 4.76Mt in 1980 to a peak of about 12.03Mt in 1996, with an annual average growth rate of 6%. However, accompanying the reduction of primary energy consumption and coal use, total NO_X emissions began to decrease after 1996. NO_X emissions decreased to a low value of 11.18Mt in 1998. This reduction is contrary to all former expectations and can be

mainly explained by the change of energy consumption mix and the lower primary energy consumption, especially the reduction of coal final consumption. Since then, NO_X emissions increased slowly again up to 11.77Mt in 2000 [5].

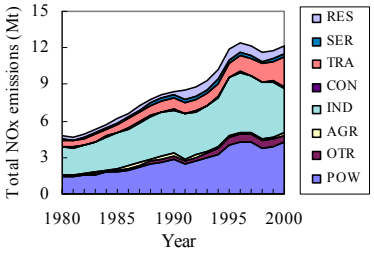

Figure 3. China's Total NO_X emissions by sectors, 1980~2000

Also, it can be seen that China's NO_X emissions is unevenly allocated in different economic sectors and fuels (see **Figure 3** and **Figure 4**). POW is the largest sources (over 1/3 of the totals), followed by IND and TRA. Similarly, Fired-Coal is the main fuel source with a share of about 63% of the totals in 2000, and followed by diesel, coke, and gasoline. In addition, China's NO_X emissions were mainly concentrated in the eastern and central provinces, accounting over 80% of the totals.

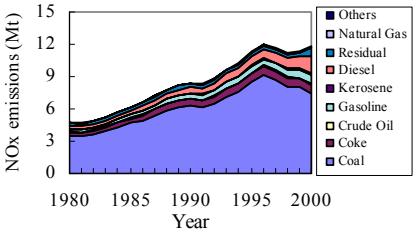

Figure 4. China's Total NO_X emissions by fuel types, 1980~2000

Trend of NO_X emissions in China. Based on different economic growth rates assumption, three scenarios of future energy demand in China were designed, which were called Low (L), Mid (M) and High (H) scenario, respectively. The assumed GDP in the future was shown in **Figure 5,** and the projected primary energy demand was shown in **Figure 6**.

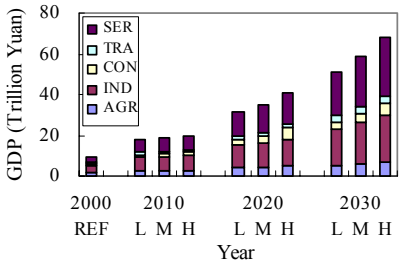

Figure 5. China's future national GDP by economic sectors

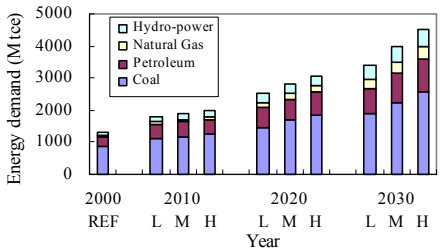

Figure 6. China's future primary energy demand by fuel types

As can be seen, the future energy demand in China will increased steadily with the rapid economic growth. By the year of 2020 and 2030, the national GDP will reach up to 31.5~50.2 trillion Yuan and 51.3~68.0 trillion Yuan, respectively. Meanwhile, the projected primary energy consumption will amount to 2528~3067Mtce and 3382~4498Mtce, respectively.

Combining the projected energy consumption with NO_X emissions factors and the assumed NO_X control efficiency, trend of NO_X emissions in China were evaluated (see **Figure 7** and **Figure 8**).

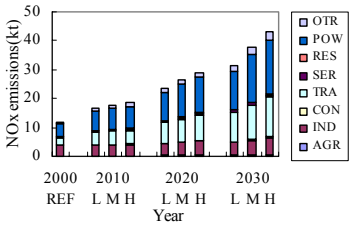

Figure 7. China's future NO_X emissions by economic sectors

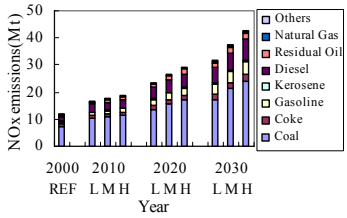

Figure 8. China's future NO_X emissions by fuel types

It can be seen that China's NO_X emissions will probably increase to about 23.6~29.1Mt in 2020 and 31.5~43.0Mt in 2030, respectively if none effective control measures were adopted. Further, China's NO_X in the future will still remain unevenly allocation among different fuels and economic sectors. By 2030, fired-coal will still be the largest fuel source, accounting for about 56% of the totals, and the share of POW, TRA and IND will be about 45%, 32% and 14%, respectively.

Conclusions

With rapid economic growth and energy consumption increase, China's NO_X emissions have reached up to a high value of 11.77Mt in 2000. If none effective control measures taken, China's total NO_X emissions will probably rise to as high as 31.5~43.0Mt in 2030, becoming the largest NO_X emission country in the world. Therefore, It is very necessary for China to regulating increasingly strict NO_X emission control standards and relevant policies as soon as possible.

Acknowledgment. This work is partially supported by the State Environmental Protection Administration (SEPA) of China under contract 98-1-01. However, the opinions expressed herein are those of the authors themselves and should not be constructed as representing the official positions of Tsinghua University, or SEPA.

References

1. Hao J.M.; Tian H.Z.; and Lu Y.Q., ES&T. **2002**, 36, 552-560
2. National Bureau of Statistics (NBS), China Statistical Yearbook 2002, China Statistical Press: Beijing, 2002.
3. NSB, China Energy Statistical Yearbook (1997-1999), China Statistical Press: Beijing, 2002.
4. Kato, N.; Akimoto, H., Atmos. Environ. **1992**, 26A, 2997-3017.
5. Streets D.G.; Waldhoff S.T., Atmos. Environ. 2000, 34, 363-374.

ADVANCED FLUE GAS TREATMNENT BY NOVEL DE-SOX TECHNOLOGY OVER ACTIVE CARBON FIBERS

*Masaaki Yoshikawa and Isao Mochida**

R & D Department, Osaka Gas Co., Ltd. 6-19-9, Torishima, Konohana-ku, Osaka554, Japan
* Institute of Advanced Material Study, Kyushu University 6-1, Kasugakoen, Kasuga-shi, Fukuoka 816, Japan

Introduction

There is a worldwide increase in the discharge of the sulfur dioxide from the use of fossil fuel. Especially in the Asia region, recent increases in the discharge are large, but environmental countermeasures have been retarded for the sake of economical efficiency. Though in the advanced nation, the limestone gypsum method is mainly used as stack gas desulphurization facility, it is the method in which both cost of equipment and operational cost are expensive.

On the other hands, it becomes obvious that SOx and NOx in flue gas can be removed at room temperature by using active carbon fibers (ACF) subjected to surface treatment such as heat treatment [1, 2]. The flue gas treatment technology using ACF is a semidry oxidation type de-SOx method that is effective even around room temperature. In addition, this technology enables by-products such as sulfuric acid, sulfates, nitric acid, and various nitrates to be recovered, and is applicable in the field of flue gas treatment to which the conventional de-SOx method, such as the limestone gypsum method, could not be applied for economical reasons.

Experimental

Characteristics of ACF catalyst

To evaluate the basic characteristics of de-SOx over ACF, comparison was made between four kinds of commercialized ACFs under the untreated condition. Table 1 shows the comparison of the properties of ACFs. Because the structures such as an external surface area, specific surface area, and pore size are unified in the manufacturing process, there is slight difference in structure of raw materials. But the compositions of raw materials significantly vary with types; phenol-type (Kuraray Chemicals Co., Ltd.) or cellulose-type (Toyobo Co., Ltd.) ACFs have high oxygen content, PAN-type (Toho tenax Co., Ltd.) ACF has high nitrogen content, and pitch-type (Adall Co., Ltd.) ACF has the largest carbon content, which indicates that the compositions of raw materials may exert great influence on the chemical properties of ACFs In order to improve the performances of desulphurization, high temperature heating treatment in the inert gas, such as nitrogen, were carried out at several conditions, described later.

Desulphurization reaction tests

Desulphurization reaction was examined in a fixed bed flow reactor at 25-50 °C , with a flow rate 400 ml/min of 1000ppm SO_2, 5% O_2, and 10-15% H_2O in N_2 over 2 g of ACF catalyst to adjust W/F (Catalyst weight by Flow rate) to 5 * 10^{-3} g min/ml. SO_2 concentration were analyzed continuously at the inlet and outlet of the reactor using Infrared SO_2 Gas Analyzer (SOA-7000, Shimadzu Co., Ltd.). Steady-state SO_2 conversion was observed when the SO_2 concentration at the outlet of the reactor became stable.

Table 1. Comparison of the properties of ACFs made of different raw materials

	Pitch type ACF	PAN type ACF	Phenol type ACF	Cellulose type ACF
Composition formula of raw materials	$[C_{124}H_{80}NO]n$	$[C_3NH_3]n$	$[C_{63}H_{55}O_{11}]n$	$[C_6H_{10}O_5]n$
Carbon content in raw material (%)	93.1	67.9	76.6	44.4
Diameter of fiber (μm)	10 to 18	7 to 15	9 to 11	15 to 19
External surface area (m^2/g)	0.2 to 0.6	0.9 to 2.0	1.0 to 1.2	0.2 to 0.7
Specific surface area (m^2/g)	700 to 2500	500 to 1500	900 to 2500	950 to 1500
Pore volume (ml/g)	0.3 to 1.6		0.22 to 1.2	
Pore diameter (nm)	to 2	2 to 4	1.8 to 4.4	1 to 1.8
Tensile strength (kg/mm^2)	10 to 20	20 to 37	30 to 40	6 to 10
Elastic modulus (kg/mm^2)	200 to 1200	7000 to 8000	1000 to 1500	1000 to 2000
Elongation (%)	1.0 to 2.8	to 2.0	2.7 to 2.8	
PH	7		7	
Ignition temperature (°C)	460 to 480	470	470	
Benzene adsorbing amount (%)	22 to 68	17 to 50	22 to 90	30 to 58
Iodine adsorbing amount (mg/g)	900 to 2200		950 to 2400	
Methylene blue decolorizing ability	to 400	to 300	to 380	

Results and Discussion

Fig.1 shows the change of de-SOx performances of commercialized four kinds of untreated ACFs with elapse of time. All the ACFs used have the same specific surface areas of about 1,000 m^2/g. The reactions were performed under the same condition that the inlet SO_2 concentration was 1000 ppm, the reaction temperature was 25°C, and water content 10%, which means super-saturated condition.

The Y-axis in the figure indicates the SO_2 breakthrough ratio (outlet SO_2 concentration / inlet SO_2 concentration). The figure shows the de-SOx activities of these four kinds of ACFs in decreasing order: pitch-type, PAN-type, phenol type, and cellulose-type ACFs. The figure also revealed that the de-SOx ratio was kept stable even after 15 hours.

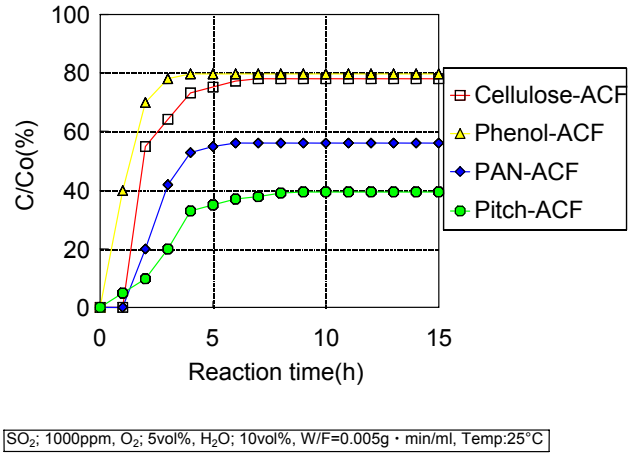

Fig. 1. Basic characteristics of de-SOx reactions over various ACFs

Like the above, the results of investigation on basic characteristics of de-SOx reaction over ACFs revealed that the pitch type ACF is most suitable for the performance. Because the four kinds of ACFs are scarcely different in structures including the specific surface area and pore size, chemical properties of them

seemed to affect the performance of de-SOx reactions. Considering that the pitch type ACF contains the largest carbon content and the least content of both oxygen and nitrogen in the raw material, and ACF with less oxygen groups may be suitable for de-SOx reactions, we investigated to achieve high perfomance of ACFs.

Therefore we devised to reduce oxygen groups of ACF as much as possible in order to accelerate this reaction. So we tried to remove the oxygen groups on the surface by carrying out high temperature heating treatment of pitch-type ACFs in the nitrogen. Fig. 2 shows the result of de-SOx when ACF with 1,060 m^2/g of specific surface area was heat treated in the temperature range from 600 to 900°C in the nitrogen. The reaction condition was nearly the same as the basic characteristics mentioned above, but the W/F (contact time) was reduced by half to 2.5 * 10^{-3} g min/ml.

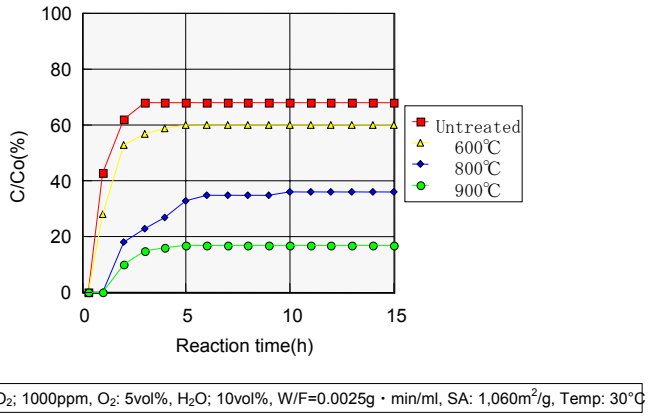

Fig. 2. Change of the de-SOx performance by heat treatment temperature

The figure clarified that the de-SOx performance was improved as the heat treatment temperature rose, and in 900°C, it reached the performance over 80%. The de-SOx performance was stable after the reaction initiation over 50 hours, and as the product material, sulfuric acid was continuously recovered. The material balance between removed SO_2 and recovered sulfuric acid agreed in the proportion over 98%.

Fig. 3 shows the summary of the result of six kinds of ACFs different in specific surface area, and the X-axis indicates the heat treatment temperature in an atmosphere of nitrogen, while the Y axis shows the de-SOx ratio. The figure revealed that de-SOx ratios of ACFs are proportional to the heat treatment temperature, and de-SOx ratio becomes higher with increasing the specific surface area. The ACF with the maximum specific surface area of 2,150 m^2/g, which was heat-treated at 900°C, showed 100% of de-SOx performance in this contact time. On the other hand, the ACF of 1000 m^2/g specific surface area stopped at 80% performance even with 900°C heat treatment temperatures.

It is considered that therefore, the performance is decided by the correlation between the improvement of the surface by the heat treatment and adsorption capacity.

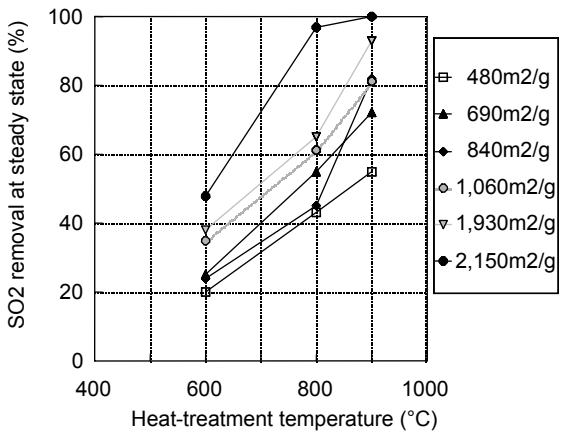

Fig. 3. Correlation between the heat treatment temperature of ACF and the de-SOx ratio

In the de-SOx over ACF, the reaction mechanism is considered like the following.

First, SO_2 is adsorbed onto the active sites on the surface of ACF, and oxidized with oxygen in flue gas into SO_3. Immediately sulfuric acid is formed by hydration of the SO_3 with water in flue gas, then, finally the sulfuric acid is absorbed in water and desorbed from the surface of ACF. In the above-mentioned reaction process, desorption of sulfric acid from the ACF surface is considered to be a rate controlling step, and therefore it is most important to increase the desorption rate. The fact that condensation of water in flue gas onto ACF doesn't inhibit adsorption of SO_2 but accelerates the reaction is the confirmation-finished by the different experiment.

On the other hand, it is also known that pore diameter and surface area of ACF do not decrease by the heat treatment at 1000°C [3]. The heat treatment increases markedly the electrical conductivity of ACF [4]. The image potential of an SO_2 molecule with the graphitic pore wall should stabilize the dipole-oriented structure in micropores of ACF, then it intensifies the catalytic activity for the SO_2 oxidation.

The oxygen function groups of ACF surface inhibits the desorption of generated sulfuric acid by its hydrogen bonding ability, and the de-SOx reaction is inhibited. Therefore, the heat treatment of pitch-type ACFs in the nitrogen removes surface oxygen functin gruops to make the hydrophobic surface, and it becomes the high activity catalyst for the desulphurization reaction.

References

1. S.Kisamori; K.Kuroda; S.Kawano; I.Mochida; Y.Matsumura; and M.Yoshikawa, Energy & Fuel, **1994**, Vol. 8, No. 6,1337
2. I.Mochida; S.Kisamori; M.Hironaka; S.Kawano; Y.Matsumura; and M.Yoshikawa, Energy & Fuel, **1994**, Vol. 8, No. 6,1341
3. T. Ohlubo; C.M.Yang; E.Raymundo-Pinero; Linares-Solano; and K.Kaneko, Chem. Phys. Letters, **2000**, 329, pp.71-75
4. M. Ruike; N.Murase; J.Imai; C.Ishii; T.Suzuki; and K.Kaneko, J. Colloid Interface Sci. **1998**, 207, pp.355

PREDICTING MERCURY SPECIATION IN COAL-DERIVED FLUE GASES

Stephen Niksa[a] and Naoki Fujiwara[b]

[a]Niksa Energy Associates, 1745 Terrace Drive, Belmont, CA 94002, neasteve@pacbell.net
[b]Coal Research Laboratory, Idemitsu Kosan Co., Ltd., Chiba 299 0267, Japan, nffish@po.iijnet.or.jp

Introduction

The coal burning utility industry is expected to mount a massive response to comply with as-yet unspecified regulations on mercury emissions from power plants that take effect in late 2007. Two Hg control technologies have already shown promise in full-scale evaluations: (1) sorbent injection with Hg recovery on particulates in ESPs or, preferably, baghouse filters; and (2) Hg recovery with the precipitated solids from wet SO_X scrubbers. Many aspects remain to be resolved, primarily because Hg control is affected by so many conditions in the power plant. Fuel quality is paramount because it determines the exhaust concentrations of acid gases (HCl, SO_2, and NO_X) and UBC, and the flyash composition – all of which affect Hg transformations. The furnace firing conditions that govern UBC emissions are the most important, whereas those that affect NO_X, moisture, and O_2 levels are secondary. The configuration of unit operations in the exhaust system determines the time-temperature history across the system, as well as when particulates are removed from the exhaust stream, as well as when the exhaust will contact catalytic agents such as SCR catalysts and filter cakes of flyash. In turn, each of these aspects affects the process chemistry. Whether or not these conditions change frequently will be determined by the operating practices of individual utility companies. Frequent coal switching accentuates the fuel quality impacts; low-NO_X retrofits accentuate the impact of furnace firing conditions; SCR installation primarily affects Hg control in systems with wet scrubbers, but would be less important for control with ESPs and baghouses.

To assist utilities sorting through the multitude of variables and equipment combinations to formulate cost-effective compliance strategies, mathematical models are being developed in parallel with the control technology. Most models rely on traditional engineering regressions of databases on Hg transformations in pilot- and full-scale testing. With the widespread dissemination of the data from 84 power plants collected under EPA's ICR program, several authors reported regressions on the effectiveness of specific unit operations for Hg control[1-4]. Unfortunately, these regressions are not statistically significant[2] (except for systems with spray dryer absorbers), due to errors and omissions in the ICR database and inadequacies in the regression functions, among many other reasons. As an example of the ambiguities, consider that, in the ICR database, the percentages of oxidized Hg at the inlets to the air pollution control devices span a range from 2 to 100 % for the most common coal-Cl levels, from 100 to 200 ppm[2]. And this excessive scatter is associated with coal-Cl, the coal property that is widely held as the determining factor on Hg transformations.

In parallel, the complexity of the Hg reaction system spawned a body of scientific observations that are now being synthesized into fundamental transformation mechanisms. These mechanisms are being expanded to describe progressively more of the interactions among exhaust species at the molecular scale. For example, the first elementary chemical reaction mechanisms for Hg oxidation were introduced in 2000[5,6]. They were then supplemented with more chemistry to quantitatively interpret the laboratory database on systems without particles in 2001, including inhibition by moisture and by NO under some, but not all, conditions[7]. In 2002, they were expanded with chemistry on UBC particles to interpret the data from coal-derived exhausts from lab-scale flames[8], and with chemistry on inorganics to generate Cl_2 from HCl[9]. They are now being expanded for the impact of sulfur species[10], and being used to predict behavior in pilot-scale coal flames, as the final prerequisite for applications in full-scale systems. The progress in developing predictive mechanisms for Hg capture on sorbents has been similarly rapid[11].

This paper surveys the development of predictive reaction mechanisms for Hg transformations in flue gases from coal-fired furnaces. Mercury oxidation is emphasized, although Hg adsorption on inherent flyash components and sorbents is recognized as an essential ingredient for any predictive capability in practical applications. Evaluations of predictions with test data are reported for progressively larger and more complex systems. To summarize the technical discussion, the reaction mechanisms are used to identify the most important fuel properties and firing practices for Hg oxidation under typical conditions in utility exhaust systems.

Mathematical Modeling

Modeling Objectives. The ultimate goal is to predict (i) the partitioning of Hg species between vapor and particulate forms and (ii) the proportions of elemental and oxidized Hg in the gas phase at the inlets to all control devices, given sets of standard coal properties, basic firing conditions, and operating conditions along the exhaust system. The partitioning onto particulates is important because adsorbed Hg can be completely collected with either ESPs or baghouses. The extent of oxidation is important because only oxidized Hg (Hg^{2+}) is water-soluble and therefore recovered in scrubbers. Also, Hg^{2+} is somewhat more difficult to collect on carbon-based sorbents. So there is a clear need for predictions (i) and (ii) at the outlets of air heaters and SCR units and the inlets to sorbent injection manifolds, ESPs, baghouses, and scrubbers. But there is less motivation to develop detailed mechanisms for SO_2 scrubbers, because full-scale testing has already established that the Hg control in scrubbers can be accurately estimated from the proportion of oxidized Hg at the inlet and the liquid-to-gas ratio of the scrubber, with secondary influence from the solution pH[4,12].

All the mercury leaving a furnace is elemental. Since the abundance of oxidized mercury expected under thermochemical equilibrium for flue gas temperatures does not materialize in actual exhaust systems, the extent of Hg oxidation from the economizer outlet through the stack inlet is determined by chemical kinetics. This oxidation primarily occurs across air heaters, while the exhaust is quenched at several hundred degrees per second, and is promoted by high concentrations of carbonaceous particles, as found in baghouse filtercakes. There is minimal Hg adsorption on particulates above 350°F, but significant recovery as temperatures are progressively reduced below this threshold. Unburned carbon is the most effective sorbent in inherent flyash, except with the flyashes from low-rank coals that contain substantial amounts of Ca. Oxidation and adsorption are not independent because UBC and high levels of Ca and Fe in flyash promote Hg oxidation, as apparent in the significant surge in the extent of oxidation across baghouse filter cakes.

Hg Oxidation Mechanism. Mercury oxidizes in three phases: in the gas phase; on particulates, especially UBC; and over SCR catalysts. The database on Hg oxidation across SCR units is just beginning to emerge and is still inadequate for mechanistic interpretations. So, in the near-term, contributions from SCRs must be estimated with correlations, which will improve as more data becomes available. But the extents of oxidation in the gas phase and over particulates can be accurately estimated with detailed mechanisms, as explained in the following two sections.

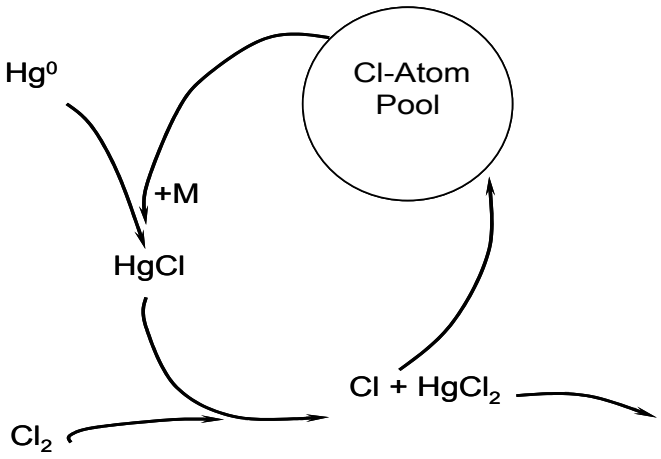

Figure 1. Cl-atom recycle during homogeneous Hg oxidation.

Homogeneous Hg Oxidation. The total amount of Hg in coal-derived exhausts is typically less than 10 ppbv. Consequently, Hg cannot possibly affect the concentrations of any of the species that participate in its own oxidation, because all are present at much higher concentrations. In other words, chemistry that does not involve Hg sets the concentrations of Cl, Cl_2, O, OH, and HO_2 that subsequently participate in the Hg oxidation. As explained elsewhere[7,8], our homogeneous mechanism includes 8 reactions for Hg oxidation that involve Hg^0, HgCl, $HgCl_2$, Cl, Cl_2, HCl, HOCl, H, and OH. This submechanism represents a Cl-atom recycle sketched in Fig. 1 whereby the Cl-atom consumed in the partial oxidation of Hg^0 into HgCl is regenerated in the subsequent oxidation of HgCl by Cl_2 into $HgCl_2$. All supporting kinetic submechanisms were taken directly from the literature and used without modification, consistent with the much higher concentrations of the species in these mechanisms. The Cl oxidation submechanism accounts for a broad range of HCl concentrations, and incorporates additional coupling of Cl chemistry and NO_X chemistry. The moist CO oxidation submechanism is an update of previous efforts by Prof. Dryer and co-workers at Princeton and describes the kinetics of moist CO oxidation at low to moderate temperatures, allowing for perturbations from NO_X conversion and interactions with NO_X and SO_X conversion chemistry. The H/N/O submechanism describes the kinetics of NO_X conversion at low to moderate temperatures. In total, 168 elementary chemical reactions are included in the homogeneous Hg^0 oxidation mechanism, without any adjustable parameters.

This mechanism alone was able to quantitatively interpret several reported datasets with synthetic flue gases without particulates[6,13-15]. As seen in Fig. 2, the mechanism accurately depicts the inhibiting effect of moisture and NO (left panel), and covers a broad range of Hg and HCl concentrations (right panel), including saturation of HCl promotion when the HCl/Hg ratio exceeds 4000.

The accuracy of these predictions notwithstanding, it soon became clear that the homogeneous mechanism alone would not be sufficient to describe Hg oxidation in utility exhaust systems. Whereas the tests behind Fig. 2 imposed gas quenching rates that were more than an order of magnitude faster than in typical air heaters, the lab tests by Mamani-Paco and Helble[15] imposed realistic quench rates. And for these conditions, the homogeneous oxidation mechanism predicted negligible extents of oxidation, in accord with the test results. More importantly, when the homogeneous Hg oxidation mechanism alone was evaluated with the measured extents of Hg oxidation for 5 coals in a lab-scale flame[16], it performed poorly, despite its success with all the available datasets with synthetic exhausts. Among these five coals, Coal D has an unusually high Cl-content and gave the most extensive Hg oxidation, as expected. In contrast, the homogeneous mechanism predicted the minimum extent of oxidation for this coal, and complete oxidation with all others. These simulations also revealed why the mechanism was failing. According to the homogeneous mechanism, Cl-atoms oxidize Hg^0 into HgCl (as seen in Fig. 1). The Cl-atom concentration develops from explosive chemistry, whereby a long induction period is needed to ignite the production of Cl-atoms at the slow quench rates in utility exhaust systems. Once this chemistry ignites, the Cl-atom concentration surges, which ultimately oxidizes most, if not all, the available Hg. This same mechanism is responsible for Hg oxidation in many of the lab-scale tests without particulates, where excessive quench rates enhanced the ignition characteristics. But it is incompatible with the moderate extents of Hg oxidation often reported for coal-derived exhausts under the operating conditions in utility exhaust systems.

Heterogeneous Chemistry. The following heterogeneous reaction subset was combined with the homogeneous mechanism to rectify the problems in the predictions for coal-derived exhausts:

$$StSA(s)+HCl \rightarrow StCl(s)+H \quad (1)$$
$$StCl(s)+Cl \rightarrow Cl_2+StSA(s) \quad (2)$$
$$StCl(s)+Hg \rightarrow StSA(s)+HgCl \quad (3)$$

There are two types of carbon sites in the mechanism: StSA(s) denotes an unoccupied site and StCl(s) denotes a chlorinated site. Unoccupied sites may be chlorinated by deposition of HCl with release of H-atoms into the gas phase, according to eq. 1. Chlorinated sites are freed either by recombination with a Cl-atom, to generate Cl_2 vapor (eq. 2), or by partial oxidation of Hg into HgCl on a chlorinated site (eq. 3). Competitive adsorption and chemistry among many other exhaust species, particularly SO_X and NO_X, were omitted for lack of kinetic information.

The proposed heterogeneous chemistry is restricted to only the carbon in the flyash. That is, in the simulations, the surface areas for heterogeneous chemistry are based on a mean size for only the suspended UBC in the entrained ash. Inorganic components of the ash do not participate. This premise would be unable to depict the distinctive Hg oxidation behavior of flyashes with elevated levels of iron oxides[17,18] or, perhaps, from subbituminous coals with high Ca levels[19]. Calcium compounds can be chlorinated by HCl adsorption[20].

As seen in Table 1, adding the heterogeneous submechanism rectified the problems in the predictions from the homogeneous mechanism alone. The improved performance reflects the much more robust activity of a chlorinated carbon surface, compared to Cl-atoms. The surface is chlorinated by HCl, the most abundant Cl-species in coal-derived exhausts, and the large storage capacity of carbon for Cl ensures that a source of Cl will be present to oxidize Hg over a broad temperature range, so initiation is not problematic.

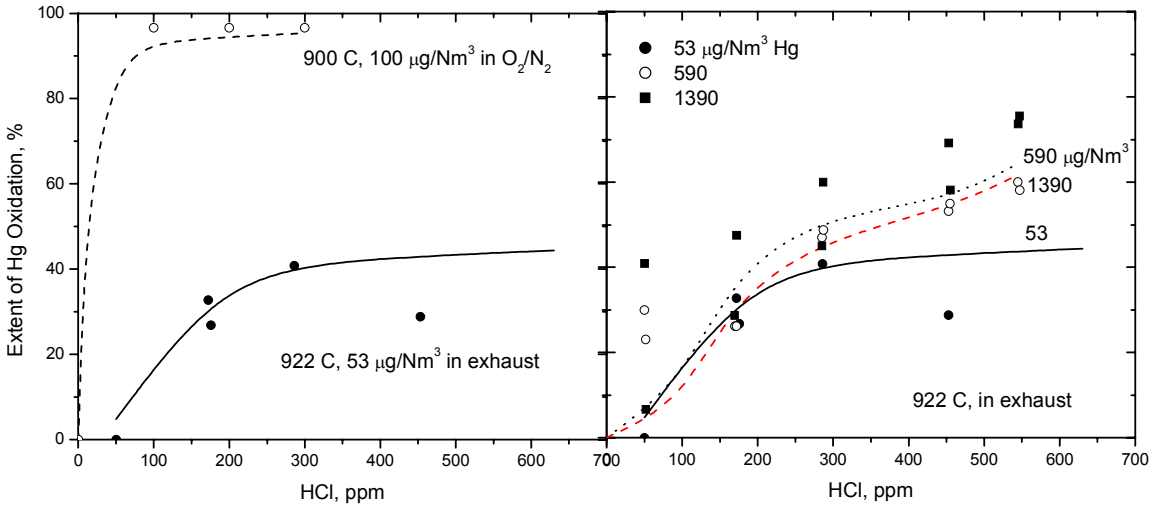

Figure 2. (Left) Comparison between extents of Hg oxidation in the absence (○) and presence (●) of water and NO; and (Right) extents of Hg oxidation for various Hg levels in exhaust prepared from natural gas combustion.

Table 1. Evaluation with flue gases from lab-scale flames.

Coal	Measured Oxidation, %	Predicted Homo/Hetero, %
A	22.8	40.2
B	48.7	42.2
C	27.5	29.6
D	93.2	71.2
E	46.5	27.6

Super-equilibrium levels of Cl-atoms are no longer necessary, so Hg is predicted to oxidize for systems with realistic quench rates. The predicted concentrations of both Cl- atoms and Cl_2were almost an order of magnitude lower than with the homogeneous mechanism only. The combined mechanism also predicted a surge in the extent of oxidation across the UBC in a final filter in the lab-scale exhaust system, consistent with the behavior in baghouse filtercakes. Most important, the predicted extents of Hg oxidation for the longest residence times were not excessive, and the complete mechanism identified the distinctive behavior of the coal with the highest Cl-content (Coal D). In addition, recent studies with x-ray absorption fine structure spectroscopy revealed Hg-Cl bonds on carbon surfaces after sorption by either Hg^0 or Hg^{2+} in synthetic flue gases that contained moisture, SO_2, and HCl[21]. Also, HCl does adsorb onto carbon at low temperatures, although the only data we found so far[22] are for activated carbon fibers with no structural similarities to UBC from a coal-fired furnace.

Input Data Requirements. The input data needed to characterize Hg oxidation in coal-derived exhausts with these mechanisms are as follows: The fuel properties consist of a proximate analysis and an ultimate analysis expanded with the Hg- and Cl-contents. The heating value is also needed whenever a furnace rating and S. R. value are used to estimate the exhaust composition leaving the economizer. Alternatively, total coal and air flowrates will also specify the moisture and CO_2 levels in the exhaust. Measured exhaust O_2 levels are much better than estimates. Complete emissions levels are required, including HCl, CO, NO_X, and SO_X. Measured values of HCl are much more reliable than estimates, due to the uncertainties on coal-Cl levels. The partitioning of flyash among bottom ash, economizer ash, and flyash is required, along with LOI data on the flyash. UBC properties (size, total surface area) are used in the analysis, but can usually be estimated from characterization data in the literature.

The essential operating conditions consist of the configuration of all unit operations in the system, and the time-temperature history from the economizer outlet to the stack. It is best to formulate a time-temperature history with temperatures at the inlet and outlet to each unit, and the nominal residence times (which can be estimated from total gas flows and unit cross sections). Finer resolution within the air heater is helpful but not usually available.

Results

Validation With a 1.0 MW_t Pilot-Scale Furnace. Mercury speciation was monitored in Southern Research Institute's Combustion Research Facility (CRF)[23]. The CRF consists of fuel handling and feeding systems, a vertical refractory lined furnace with a single up-fired burner, a horizontal convective pass, several heat exchangers in series and a baghouse filter. Emissions from this system have been qualified against those from full-scale, tangential-fired furnaces for the operating conditions imposed in this work[24]. The 8.5 m by 1.07 m (i.d.) cylindrical furnace handles gas velocities from 3 to 6 m/s, and residence times from 1.3 to 2.5 s. The nominal firing rate is 1.0 MWt, which was fixed for all cases. A single burner generates a core of pulverized fuel and primary air surrounded by weakly swirled secondary air. Overfire air (OFA) was injected through 4 off-radius ports located 4.6 m down the furnace. The gas temperature history along the exhaust system compares very well with the histories assigned from temperature profiling on full-scale systems.

Mercury speciation was monitored with a PS Analytical Hg detector using samples extracted from the flue gases with an Apogee Scientific QSIS probe. Two sampling positions were used to monitor the speciation at 163 and 280°C. In addition, all major flue gas species were measured, including HCl, SO_2, CO_2, CO, NO_X, SO_X, and O_2. Both LOI and UBC levels were determined for the flyash. LOI was used in all calculations, for consistency with the other evaluations with data completed to date. The test procedures are more completely described elsewhere[23].

Table 2. Evaluation with flue gas from a 1.0 MW_t furnace.

Coal	Coal-Cl, daf wt. %	LOI, wt. %	Hg Oxidation, %	
			Pred.	Mes'd
Bit. #1	0.010	4.8	74.8	76.0
Bit. #1/H_2O	0.010	4.8	72.0	63.0
Bit. #2	0.013	4.2	50.0	52.0
PRB	0.013	0.2	18.9	18.7
PRB	0.013	0.2	29.0	30.0

Two test series are included in the model validations. The baseline firing conditions were imposed on three coals, including two Eastern bituminous and a PRB subbituminous. Steam injection into the burner was applied with one of the bituminous coals. In the second test series with PRB, Cl_2 was injected at two concentrations where the flue gases were at 573°C, upstream of the heat exchangers. It is important to realize that the test conditions were directly imposed in all simulations, and none of the model parameters were adjusted in any of these cases. The characteristics of UBC in the simulations were specified from the reported LOI levels and characterization data in the literature. For cases with LOI levels under 1 %, the nominal UBC size was adjusted downward for consistency with char burnout predictions. Otherwise, the reported flue gas composition and exhaust thermal history were imposed without modification.

As seen in Table 2, the predictions are remarkably accurate for all three coals. Both bituminous coals have substantially higher extents of Hg oxidation than the PRB, as expected. But Bit. #1 also has significantly more oxidized Hg than Bit. #2 despite similar coal-Cl and LOI levels. Both bituminous coals had unusually low Cl-levels which were either equal or below the PRB's so, clearly, coal-Cl is not the determining factor in Hg oxidation. The mechanism depicts the large variations due to coal quality within experimental uncertainty throughout, based primarily on the substantial variations in the LOI levels. The impact of steam injection is also evident in the predictions, albeit only qualitatively.

To simulate cases with Cl_2 injection on PRB-derived flue gas, Cl_2 concentrations of 9, 17, and 69 ppm were instantaneously imposed in the simulations at the point where the exhaust temperature was 573°C. In all cases, the predicted extent of Hg oxidation at the injection position was zero. However, Hg was predicted to oxidize immediately thereafter. As seen in Fig. 3, the predicted extents of Hg oxidation are essentially within the ranges assigned from the tests (as indicated by the error bars) for the whole coal (at 0.9ppm Cl_2) and for both cases with Cl_2 injection. The slight overpredictions for both of the tested Cl_2 levels are expected from the omission of finite-rate mixing, which could easily be rectified. Insufficient data is available to validate the predicted saturation for high Cl_2 levels.

Predictions for Coal-Fired Utility Exhaust Systems. The complete Hg oxidation mechanism was used to simulate various fuel and exhaust properties under typical operating conditions. The baseline fuel is an eastern high volatile bituminous coal with 0.1 ppm Hg and 100 ppm Cl. The overall stoichiometric ratio for the furnace was 1.19. As seen in Fig. 4, variations in both coal-Cl and coal-Hg are most important for the low end of either range, then these effects saturate at the highest levels that arise in practical applications. For these particular simulation conditions, coal-Cl becomes unimportant for levels above 0.15 wt. %, which is near the upper limit on typical coal-Cl levels. Whereas the predicted extents of Hg oxidation become more sensitive for progressively lower coal-Cl levels, they

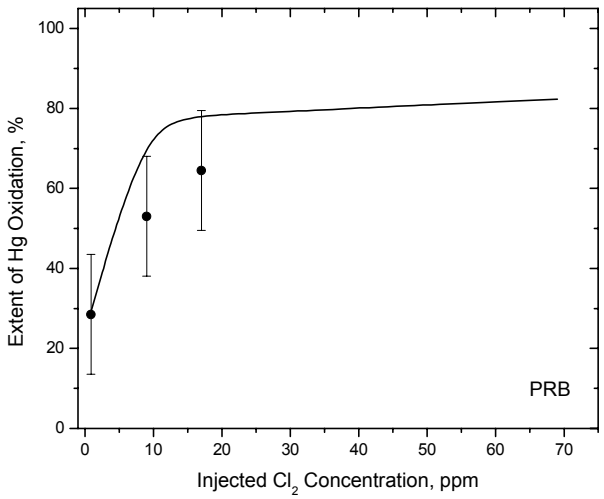

Figure 3. Evaluation of predicted extents of Hg oxidation with Cl_2 injection.

do not vanish until, strictly speaking, all Cl has been eliminated from the reaction system. Cases with 0.001, 0.005, and 0.02 % coal-Cl correspond to exhaust HCl concentrations of 0.6, 2.8, and 11.2 ppm. The predicted extents of Hg oxidation for these respective cases increase from 67 to 71 to 82 %, a net change of 15 %.

The impact of variations in coal-Hg appears to cover a similar range in Fig. 4 but, in fact, the plotted range of coal-Hg values is greater than the actual range of reported values. It is extremely unusual to find coal-Hg values greater than 0.2 ppm, or less than 0.05 ppm. Within this restricted range of coal-Hg, this parameter is a relatively weak influence on the extent of Hg oxidation.

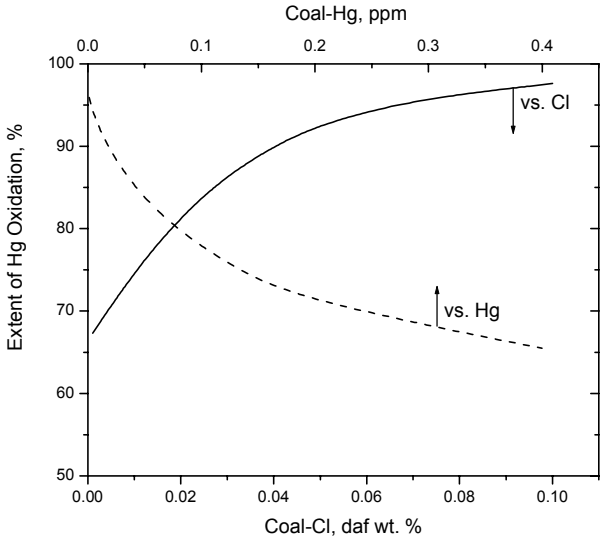

Figure 4. Predicted sensitivities to coal-Cl (solid curve) and coal-Hg (dashed curve) for baseline conditions with hv bit coal.

The strongest impact of all is seen with variations in the UBC level, which appears in Fig. 5. As the UBC was increased from 0.1 to 7 wt. %, the predicted extents of Hg oxidation increased from 5 to 90 %. Indeed, the single most important reason for the extensive Hg oxidation in the flue gases from hv bit coals is their relatively high UBC levels. The variation with the mean UBC size is due to the role

of UBC surface area in the oxidation mechanism. Based on detailed characterization studies of the characteristics of UBC from p. f. flames[25], we expect the UBC size to be significantly larger than the size of the coal feed, unless LOI is less than 1 wt. %.

The predicted impact of variations in exhaust O_2 and NO indicated that both factors are among the least important in this reaction system, provided that all else remains the same. In practice, variations in both O_2 and NO are almost always associated with substantial changes to UBC levels. But at a fixed UBC level, variations in O_2 levels are usually inconsequential, and variations in NO levels are only important for levels below 200 ppm, which are rarely encountered with large-scale flames.

Predictions for variable quench rates were prepared for ± 30 % variations around the mean quench rate. The predicted extents of Hg oxidation increase for slower quench rates in this range, from 59 % with fast quenching to 74.8 % for the baseline quench rate to 93.5 % for the slowest quench rate. So the time-temperature histories across the exhaust system must be specified within fairly close tolerances.

Summary

A heterogeneous reaction mechanism is needed to initiate Hg oxidation under utility exhaust conditions, and also to sustain the partial oxidation of Hg into HgCl. The heterogeneous Hg mechanism described here represents the chlorination of carbon in the ash by HCl, with subsequent recombination of Cl-atoms and partial oxidation of Hg into HgCl on the chlorinated sites. In conjunction with the original homogeneous reaction mechanism, it depicts the observed coal quality impacts in the exhausts from lab- and pilot-scale flames within useful quantitative tolerances without heuristic adjustments to the kinetic parameters or operating conditions.

The same homogeneous mechanism previously interpreted all the available datasets on Hg oxidation in synthetic exhausts, without particulates. But when the homogeneous reaction mechanism was applied to the conditions in the exhaust systems of coal-fired furnaces, where quench rates are much slower, several problems surfaced. Without rapid quenching, Cl-atom concentrations usually remained below the threshold for initiation of Hg oxidation. And in cases with appreciable Hg oxidation, the oxidation persisted through the lowest temperatures in the simulations, because the rate of Cl-atom recombination is slow. In the evaluation with the lab-scale coal flame data, this problem became apparent as essentially complete Hg oxidation for the longest residence times with four of the five coals, which was contradicted by the data and by the reported coal quality impacts.

Adding the heterogeneous submechanism rectified these problems by supplanting Cl-atoms with a chlorinated carbon surface. The surface is chlorinated by HCl, the most abundant Cl-species in coal-derived exhausts, and the large storage capacity of carbon for Cl ensures that a source of Cl will be present to oxidize Hg over a broad temperature range, so initiation is not problematic. Super-equilibrium levels of Cl-atoms are no longer necessary, so Hg is predicted to oxidize for systems with realistic quench rates. The predicted concentrations of both Cl-atoms and Cl_2 were almost an order of magnitude lower than with the homogeneous mechanism only.

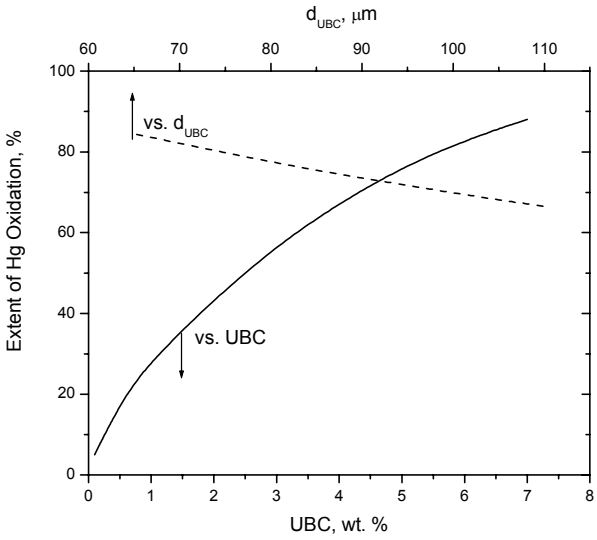

Figure 5. Predicted sensitivities to the level (solid curve) and mean size (dashed curve) of UBC for baseline conditions with hv bit coal.

Adding the heterogeneous submechanism also provides the basis for a truly predictive capability, and interprets some of the more perplexing aspects of Hg oxidation seen in full-scale test data. In the CRF datasets, the reported extents of Hg oxidation ranged from 20 to 75 % even though the coal-Cl contents were essentially uniform. Whereas this broad range is similar to the large spread seen in the ICR database for similar coal-Cl contents, it is even more compelling because strictly the same firing conditions were imposed on all coal types and all relevant operating conditions were accurately recorded. The complete mechanism depicts these variations within experimental uncertainty without any parameter adjustments, and also identifies LOI variations as their predominant underlying cause. From a practical standpoint, this finding implies that high LOI levels will compensate for low coal-Cl and vice versa. Hence, subbituminous coals exhibit the lowest extents of Hg oxidation whenever both their Cl-contents and LOI levels are very low, as with the PRB in the CRF tests. Indeed, simply spiking the PRB-derived flue gases with Cl_2 almost completely oxidized the Hg even while the LOI remained very low. Our mechanism quantitatively interpreted this behavior, which paves the way for an important supporting role for modeling in the development of more effective Hg control processes. Evaluations of the mechanism with data from full-scale tests are already underway.

Acknowledgement. This study was partially sponsored by the New Energy Development Organization's (NEDO) Clean Coal Technology Center under the Toxic Metals Project, and administered by the Coal Research Laboratory, Idemitsu Kosan Company, Ltd. Supplemental funding to interpret the CRF datasets was provided by Southern Research Institute under their EPRI-sponsored "Mercury Chemistry" project.

References

(1) Chu, P.; Behrens, G.; Laudal, D., Proc. U. S. EPA-DOE-EPRI Combined Power Plant Air Pollutant Control Symp.: The Mega Symp. and AWMA Specialty Conf. on Mercury Emissions: Fate, Effects, and Control, 2001, Chicago, IL, Aug. 21-23.

(2) Afonso, R.; Senior, C., Proc. U. S. EPA-DOE-EPRI Combined Power Plant Air Pollutant Control Symp.: The Mega Symp. and AWMA Specialty Conf. on Mercury Emissions: Fate, Effects, and Control, 2001, Chicago, IL, Aug. 21-23.

(3) Berkenpas, M. B.; Rubin, E. S.; Smith, D. N.; Gibbon, G. A.. Proc. U. S. EPA-DOE-EPRI Combined Power Plant Air Pollutant Control Symp.: The Mega Symp. and AWMA Specialty Conf. on Mercury Emissions: Fate, Effects, and Control, 2001, Chicago, IL, Aug. 21-23.

(4) Weilert, C. V.; Randall, D. W., Proc. U. S. EPA-DOE-EPRI Combined Power Plant Air Pollutant Control Symp.: The Mega Symp. and AWMA Specialty Conf. on Mercury Emissions: Fate, Effects, and Control, 2001, Chicago, IL, Aug. 21-23.

(5) Widmer, N.C.; West, J.; Cole, J.A., Proc. A&WMA Annual Conf., 2000, Salt Lake City, AWMA, Pittsburgh.

(6) Sliger, R. N.; Kramlich, J. C.; Marinov, N. M., Fuel Process. Technol. 2000, 65-66(0), 423-438.

(7) Niksa, S.; Helble, J. J.; Fujiwara, N., Environ. Sci. Technol. 2001, 35, 3701-3706.

(8) Niksa, S.; Fujiwara, N.; Fujita, Y.; Tomura, K.; Moritomi, H.; Tuji, T.; Takasu, S., J. A&WMA 2002, 52(8):894-901.

(9) Edwards, J. R.; Srivastava, R. K.; Lee, C. W.; Kilgroe, J. D.; Ghorishi, S. B., Proc. U. S. EPA-DOE-EPRI Combined Power Plant Air Pollutant Control Symp.: The Mega Symp. and AWMA Specialty Conf. on Mercury Emissions: Fate, Effects, and Control, 2001, Chicago, IL, Aug. 21-23.

(10) Qiu, J.; Helble, J. J., "Development of an Improved Model for Determining the Effects of SO_2 on Homogeneous Hg Oxidation," 28th Int. Technical Conf. on Coal Utilization and Fuel Systems, 2003, Coal Technology Assoc., Clearwater, Fl, March.

(11) Sjostrom. S.; Ebner, T.; Ley, T.; Slye, R.; Richardson, C.; Machalek, T.; Richardson, M.; Chang, R., J. A&WMA 2002, 52, 902-911.

(12) DeVito, M. S.; Rosenhoover, W. A.; Proc. A&WMA Annual Conf. 1999, St. Louis, AWMA, Pittsburgh, Paper No. 99-33.

(13) Widmer, N. C.; Cole, J. A.; Seeker, W. R.; Gaspar, J. A. Combust. Sci. Tech. 1998, 134, 315-326.

(14) Hall, B.; Schager, P.; Lindqvist, O. Water, Air, and Soil Pollution 1991, 56, 3-14.

(15) Mamani-Paco, R. M.; Helble, J. J. Proc. A&WMA Annual Conf., 2000, Salt Lake City, AWMA, Pittsburgh.

(16) Fujiwara, N.; Fujita, Y.; Tomura, K.; Moritomi, H.; Tuji, T.; Takasu, S.; Niksa, S., Fuel, 2002, 81(16):2045-52.

(17) Norton, G. A.; Yang, H.; Brown, R. C.; Laudal, D. L.; Dunham, G. E.; and Okoh, J. M., Proc. A&WMA Annual Conf. 2000, Salt Lake City, AWMA, Pittsburgh, Paper No. 00-167.

(18) Lee, C. W.; Kilgroe, J. D.; and Ghorishi, S. B., Sixth Annual Waste-to-Energy Conf. 1998, p. 221-238.

(19) Carey, T. R.; Hargrove, O. W.; Richardson, C. F.; Chang, R.; and Meserole, F. B., Proc. A&WMA Annual Conf. 1997, AWMA, Pittsburgh, Paper No. 97-WP72A.05.

(20) Ghorishi, B.; Gullett, B. K.; Jozewicz, W.; and Kozlowski, W., EPRI-DOE-EPA Combined Utility Air Pollution Control Symposium: The MEGA Symp. 1999, EPRI, p. 19-59.

(21) Huggins, F. E.; Huffman, G. P., Energy Fuels 1999, 13(1):114.

(22) Mangun, C. L.; Benak, K. R.; Economy, J.; and Foster, K. L., Carbon 2001, 39:1809-1820.

(23) Gale, T.; Cushing, K., EPRI-DOE-EPA-A&WMA Combined Utility Air Pollution Control Symposium: The MEGA Symp. 2003, EPRI, to appear.

(24) Monroe, L. S. et al., EPRI-DOE-EPA Combined Utility Air Pollution Control Symposium: The MEGA Symp. 1995, Book 3, EPRI, Palo Alto, CA.

(25) Hurt, R. H.; and Gibbins, J. R., Fuel 1995, 74(4):471-480.

Evaluation of Mercury Stability in Ontario Hydro Method Solutions for Mercury Speciation in Flue Gas Generated from Coal-Fired Stationary Sources

Jenny Q. Sun, Karen S. Uhrich and Richard L. Schulz

Energy & Environmental Research Center
University of North Dakota
PO Box 9018
Grand Forks, North Dakota 58202-9018

Abstract

In 1994, the Ontario Hydro (OH) mercury speciation sampling method began development and eventual validation. This method, initially proposed by Dr. Keith Curtis of Ontario Hydro, was shown to provide reliable mercury speciation results. As a result, a draft American Society for Testing and Materials (ASTM) method was issued in 1998(1).

The stability of mercury in the OH solutions depends on the various reagents added into solutions during the breakdown. The amount of these reagents is not stated very clearly in the method, rather it depends on experienced people performing the breakdown. This would result in the variation of the sample solution conditions and subsequently affect the mercury stability. The research presented here addresses some of these concerns.

Background

The 1990 Clean Air Act Amendments (CAAAs) required the U.S. Environmental Protection Agency (EPA) to determine whether the presence of mercury in the stack emissions from fossil fuel-fired electric utility power plants poses an unacceptable public health risk. EPA's conclusions and recommendations were presented in the *Mercury Study Report to Congress* and *Utility Air Toxics Report to Congress* (2). The first report addressed both the human health and environmental effects of anthropogenic mercury emissions, while the second addressed the risk to public health posed by the emission of mercury and other hazardous air pollutants from steam electric-generating units. Although these reports did not state that mercury controls on coal-fired electric power stations would be required, they did indicate that EPA views mercury as a potential threat to human health. Therefore, it was concluded that mercury controls at some point might be necessary. EPA also indicated that additional research information was necessary before any definitive statement could be made. In an effort to determine the amount and types of mercury being emitted into the atmosphere by coal-fired power plants, EPA issued an information collection request (ICR) in late 1998. In addition to requiring all coal-fired power plants to measure and report their coal mercury concentrations, 80 power stations were required to measure the speciated mercury concentration in the flue gas. The method chosen by EPA for measuring speciated mercury in the stack gas was the Ontario Hydro (OH) mercury speciation method.

Beginning in 1994, the Energy & Environmental Research Center (EERC), with funding from EPRI and the U.S. Department of Energy, helped to develop and eventually validate the OH mercury speciation sampling method. Initially, the method was only used by research organizations with highly trained people. However, when EPA issued the ICR a number of sampling organizations and laboratories with varying degrees of training and experience began using this method. It is clear that if this method is going to be used on a regular basis, understanding of each step of this method rather than personal experience or interpretation of the method is imperative.

The OH method (Figure 1) consists of three KCl solution impingers, one HNO_3–H_2O_2 solution impinger, three $KMnO_4$–H_2SO_4 solution impingers, and a silica gel desiccant in sequence. The coal combustion flue gas passes through KCl first, then H_2O_2, and finally $KMnO_4$. The oxidized mercury presumably will be trapped in the KCl solution, and the elemental mercury will be trapped in the $KMnO_4$ solution. The mercury trapped in the H_2O_2 solution is considered elemental mercury and will be added to the mercury portion from $KMnO_4$ in the final calculation. The saturated $KMnO_4$ (about 5%) solution was added to the KCl during the breakdown to remove SO_2 by the reaction between $KMnO_4$ and SO_2. The method states that the purple color should remain for at least 15 minutes. In the initial design of OH method, hydrochloric acid was added at the end of break-down to rinse off the KCl and $KMnO_4$ impingers preserving the mercury in sample solutions. This step released chlorine gas due to the reaction between HCl and $KMnO_4$, and chlorine is considered hazardous to the operators. A later-modified procedure calls for 10% hydroxylamine solution to replace the hydrochloric acid. This approach eliminated the chlorine gas problem; however, it also reduced the acidity of KCl solution and chloride concentration in $KMnO_4$.

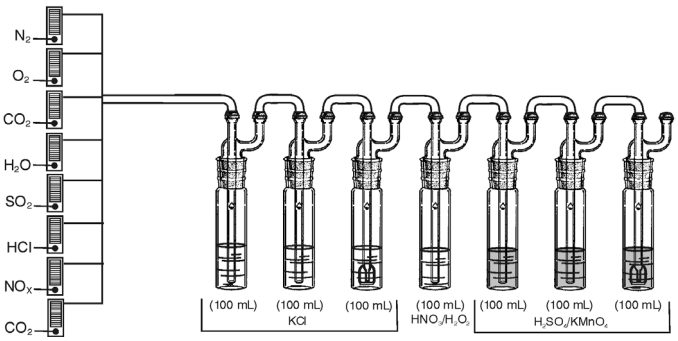

Figure 1. OH method impinger train.

The OH method results could be used directly to evaluate the mercury species at the sampling points and compare or confirm the continuous emission monitor's (CEM) performance. In either case, accurate results are crucial for the researchers to make subsequent decisions or justifications of the following work. When field crews were equipped with a cold-vapor atomic absorption (CVAA) mercury analyzer on-site, the samples could be analyzed shortly after the samples were collected. In some cases, the samples were analyzed on-site, and some duplicates had to be sent to another lab for analysis as a mean of quality assurance/quality control. When the CVAA analyzer has not been available on-site, the collected samples have to be sent to another lab for analysis. The delivery can take several days or even weeks because the samples are considered hazardous material and must be shipped on the ground. The stability of mercury in these solutions becomes a concern as the results show bias low or a faded purple color of the solution. The maximum holding time for each kind of solution has not been addressed in the method.

The following questions outline the concerns regarding the stability of mercury in OH method solutions:

- It is well known that mercury is very stable in the solutions where chloride is present and the solution is acidic. Mercury in 10% hydrochloric acid could last for years

without degrading. In general, after the breakdown, the KCl solution would have a low pH value because of the acid gases in the flue gas dissolved in the KCl solution and the additional 10% nitric acid added. The problem is that most of time the amount of 10% nitric acid was limited by the significant amount of water from the flue gas moisture during the sampling period and the amount of hose-rinsing water. Both have to be combined with the KCl solution in the final volume (500mL). To avoid overflowing, operators have to reduce the amount of 10% nitric acid. By doing so, will the stability of mercury in solution be compromised? A minimum amount of 10% nitric acid should be established to ensure mercury is maintained in the solution under any sampling process.

- According to the method, the $KMnO_4$ solution should be added to the KCl solution during the breakdown until the purple color persists for 15 minutes to neutralize any SO_2 that may be dissolved in the KCl solution. Since "purple" is not a clear-cut value for the oxidizing strength measurement, how much purple has to be provided to sustain mercury and prevent the slow reaction between SO_2 and $KMnO_4$ afterwards? If the color becomes brown or pink instead of purple, is it an indication of solution degrading and mercury disappearing?
- When samples need to be shipped after the breakdown, the samples are usually treated without further reducing the $KMnO_4$, assuming that $KMnO_4$ preserves the mercury in solution. This raises two issues: first, it costs much more for shipping and handing because $KMnO_4$ is considered an oxidizer and explosive hazardous material and, second, it is not known whether $KMnO_4$ or other components preserve the mercury. Which components in the solution are crucial for mercury preservation? In which solution is mercury more stable, in non-reduced or reduced solution*?*

Two solutions, KCl and $KMnO_4$, will be evaluated here since more than 95% of mercury is trapped in these two solutions.

Experimental

Table 1 summarizes the simulated flue gas conditions for generating OH method blank solutions for further spiking tests. Simulated flue gas component concentrations were chosen to represent high- and low-sulfur coals combusted in U.S. power plants. Moisture was not used in these tests since it is irrelevant to this study.

Table 1. Simulated flue gas component concentrations

	O_2	CO_2	SO_2	HCl	NO_2	NO
high sulfur coal	6%	12%	2500ppm	50ppm	15ppm	300ppm
low sulfur coal	6%	12%	200ppm	50ppm	15ppm	300ppm

After the simulated flue gas passed through the impingers for 1 hour, the solutions were transferred to 500-mL volumetric flasks. The mercury was spiked into the volumetric flask. The solutions were treated under controlled conditions that are summarized in Table 2.

A schematic of the bench-scale testing system and the impinger train used in this study is shown in Figure 1. All tests were sampled at a total flow rate of 30 standard cubic feet per hour (scfh) for a period of 1 hr. All of the components of the simulated flue gas were generated from a compressed cylinder. As shown in Figure 1, the gas flow was controlled by a mass flow controller and passed through a heated gas manifold to the OH method train.

All of the samples generated were analyzed by a CETAC M6000A CVAA spectrometer at wavelength 254 nm.

All of the chemical reagents used in this study were analytical grade.

Table 2. Preserving Conditions

Test for KCl portion	high sulfur				low sulfur			
	1	2	3	4	1	2	3	4
add $KMnO_4$ barely enough	x				x			
add $KMnO_4$ barerly enough+ additional 5mL						x		
add $KMnO_4$ barerly enough+ additional 10mL			x				x	
No 10% HNO_3 rinse only $KMnO_4$ -15mL				x				x
	high sulfur				low sulfur			
Test for $KMnO_4$ portion	1	2	3	4	1	2	3	4
2-3 mL of hydroxylamine chloride	x				x			
2-3 mL of hydroxylamine chloride		x				x		
2-3 mL of hydroxylamine chloride			x				x	
no hydroxylamine chloride added				x				x

Results and Discussion

To evaluate the effect of SO_2 on mercury stability in OH method solutions, simulated high- and low-sulfur coal flue gases were used for comparison. Comparing the mercury reading over the 2 weeks of low and high SO_2 under the condition of without adding any 10% HNO_3 during the breakdown, the mercury in the low-SO_2 KCl solution started to decrease after 22 hours but not in the high-SO_2 KCl solution. It indicates that the high concentration of SO_2 in flue gas might lowers the pH of the KCl solution to an adequate level to preserve mercury without additional 10% HNO_3. However, it should be pointed out that, because SO_2 in flue gas can only be estimated, the minimum quantity of 10% HNO_3 for 500 mL KCl solution should be established to sustain mercury.
50 mL of 10% nitric acid, based on the results from this experiment, can be used as a guideline.

To determine the stability of mercury in both reduced and non-reduced solutions, the samples were split into two portions after mercury had been spiked. One portion was kept as is, and the other portion was reduced 1 hr after sampling by either hydroxylamine chloride or hydroxylamine sulfate addition until the solution was colorless. The results from both high- and low-SO_2 concentration tests show that there is no mercury degradation on the reduced solution portion. This means the samples are not considered hazardous materials. This could considerably reduce the cost of shipping and make it much easier for handling the solutions as well. These tests proved that mercury could be preserved well after the $KMnO_4$ in solutions had been reduced, as long as the sample was properly treated beforehand. The other motivation for promoting the sample's reduction is that without the $KMnO_4$ in the solutions, the sample solutions do not let off chlorine gas, which is harmful for the operators.

It was noticed that there were some color changes in the KCl solutions when $KMnO_4$ was added, leaving little purple. The purple color disappeared after 1 day and a brown fluffy precipitate formed. The mercury readings for the period over 3 weeks in these bottles show no significant difference from those with more $KMnO_4$. This suggests that excess amounts of $KMnO_4$ may not be necessary during the breakdown.

Conclusions

- It should be stated clearly in the OH method that hydroxylamine chloride has to be used for $KMnO_4$–H_2SO_4 solution rather than any kind of hydroxylamine because mercury can be given off as a gas after $KMnO_4$ is reduced without the presence of chloride in solution. Even though the method calls for few drops of hydroxylamine chloride solution during the breakdown, it still provides some degree of preservation for mercury. 2–3 mL hydroxylamine chloride was used in this experiment, and the result showed this is an adequate amount for stabilizing mercury in the $KMnO_4$ solution.
- The acidity of the KCl solution is very crucial for mercury preservation, especially when low-sulfur coal is burned. Even with the $KMnO_4$ added to the solution, the amount of 10% nitric acid should be no less than 50 mL for 500 mL of KCl solution.
- When samples are treated properly during breakdown, they can be reduced to a colorless solution afterward to avoid the difficulty of storage, shipping, or handling without jeopardizing the mercury stability.

References

ASTM D 6784-02 Standard Test Method for Elemental, Oxidized, Particle-Bound and Total Mercury in Flue Gas Generated from Coal-fired Stationary Source (OH Method)

(1) Hunt, J. E.; Winans, R. E.; Ahrens, M.; and Xu, L. Prepr. Pap. - *Am. Chem. Soc., Div. Fuel Chem.*, **1999**, *44* (3), 610.

(2) Beck, J. S.; Vartuli, J. C.; Roth, W. J.; Leonowicz, M. E.; Kresge, C. T.; Schmitt, K. D.; Chu, C. T-W.; Olson, D. H.; Sheppard, E. W.; McCullen, J. B.; Higgins, J. B.; Schlenker, J. L. *J. Am. Chem. Soc*. **1992**, *114*, 10834.

(3) Winans, R. E. In *Advances in Coal Spectroscopy*; Meuzelaar, H.L.C, Ed.; Plenum Press: New York, 1992; pp. 255-274.

Mercury combustion chemistry resolved: A new mitigation approach

Keith Schofield

Materials Research Laboratory, University of California, Santa Barbara, CA 93106

Introduction

Trace levels of mercury compounds in any high temperature process volatize as elemental atomic mercury. This is unreactive in the gas phase and is largely exhausted as atoms into the atmosphere. Its emissions are difficult to control, as absorbers and other methods are not very effective at retaining the atoms of its very volatile condensed liquid phase. This behavior stems from the somewhat unique chemistry of mercury. In the gas phase it displays mainly very weakly bound molecules such as its oxide, hydroxide and monohalides. Its only stable gaseous molecule of significance in combustion is mercuric dichloride. This is exceptional having a first bond strength of about 360 kJ/mol. However, at high temperatures, although thermodynamically favored, the formation is kinetically restricted and no direct channels exist. The intermediates that would be necessary for its formation are not stable. Nevertheless, what is observed in practice is that a small fraction of the mercury in exhaust gases is present as the dichloride. This and the atomic mercury appear to constitute the elements mass balance. Extensive kinetic modeling studies have failed to satisfactorily explain this occurrence and generally have concluded that the chemistry is more complex[1,2] . Although numerous experiments have endeavored to find a correlation between this fractional degree of conversion and some operational parameter, nothing has emerged. The data are inconsistent and there is no satisfactory explanation why the ratio varies, is unpredictable, and how the conversion occurs. The very important practical aspect of such a conversion is that whereas atomic mercury emissions are difficult to control, the dichloride is readily soluble in water.

Because the chemistry of mercury starts in the high temperature gases and ends in the exhaust gas phase it has always been considered a gas phase phenomenon. Moreover, condensed phase mercury is a very volatile liquid. In the exhaust gases from coal combustors the traces of mercury are on a parts per billion by volume scale implying that conditions will always be above the dew point. Condensation of mercury would appear to be out of the question. As a result, the combustion chemistry of mercury has always been limited to considering a dominance of gas phase reactions.

In previous studies in this laboratory it was found that if sodium and sulfur are present in flame gases at very low levels (ppmv) that sodium sulfate forms very efficiently not in the flame gases themselves but on a cooled surface intercepting the flows[3,4]. The reduced dimensionality of the surface facilitates the process as well as changing the chemistry from the gas phase to the condensed phase regime. Moreover this chemistry is dominated by the surface, utilizing the gases solely as a source of ingredients and also disregards any concepts of dew point. Based on this background it was decided to run several test experiments with low levels of mercury in the burned flame gases and see if any deposition might occur on a cooled probe immersed in the exhaust. The very first experiment yielded an abundant yellowish deposit with a rate of deposition (atoms/s) essentially the same in magnitude to those collected in alkali sulfate[3,4] or carbonate deposit[5] experiments. Obviously mercury has a significant heterogeneous chemistry that has never been examined. This presentation outlines the results of this first quantitative examination of the nature of these deposits and determines the major controlling parameters in such systems.

Experimental

Flame Deposition Methods. A flat flame atmospheric pressure burner produces a one-dimensional cylindrical flame surrounded by an identical shielding flame. The inner flame is used as the experimental laminar plug flow medium containing the additives[4]. Propane, oxygen, nitrogen flames have been used over a range of fuel lean and rich equivalence ratios. Mercury is introduced into the inner flame unburned gas flow as a fine aqueous aerosol from an ultrasonic nebulizer. Solutions of mercuric nitrate or acetate at strengths of 0.008 to 0.05 N have been used and produce concentrations of atomic mercury in the burned gases of up to about 30 ppmv. Such levels produce deposition rates of several milligrams of mercury per hour. Differing flame concentrations are obtained by varying the solution strength. Small quantities of sulfur or chlorine also can be added using certified gas cylinder mixtures of 0.1% SO_2 in N_2, 514 ppmv Cl_2 in N_2, and 998 ppmv HCl in N_2. Calibrated electronic mass meters control all the gas flows.

Several cylindrical collection probes have been used. These are about 12 mm in diameter which is about the same size as the inner flame. They are of Inconel-600 stainless steel with a central channel for air or water-cooling. A thermocouple built into the wall thickness monitors surface temperature. One probe is tightly clad with a two-micron thick foil of platinum. A probe is held horizontally in the vertical flame burned gas flows and the burner raised or lowered to examine downstream location effects. Important additional experiments have utilized probes that can be internally heated. Also of Inconel stainless steel these have been useful in facilitating numerous experiments that more realistically simulate the cooler exhaust gas chemistry and also for measuring ablation rates of deposits with traces of different flowing reactive gases. The unheated probes have examined behavior at downstream times of about 5-15 ms whereas the heated probes were located at about 0.1 s downstream where the burned gases of these flames have cooled to about 200 ^oC. Probe temperatures have been in the range 55-400 ^oC.

Characterization Methods. A powerful combination of four analytical techniques has permitted an essentially total analysis of the observed deposition, erosion and conversion processes. A Nicolet Fourier Transform Raman Spectrometer has been used to obtain the Raman spectra of some deposits and their x-ray spectra also have been obtained on a Bruker High Temperature Powder X-Ray Diffractometer. Quantitative analyses have utilized a Thermo Jarrell Ash Inductively Coupled Plasma/Atomic Emission Spectrometer (ICP/AES). For this, deposits are dissolved off the probe with dilute nitric acid and can be analyzed for both their mercury and sulfur content. This provides for very accurate quantitative data. To assess the thermal stabilities of various mercury compounds, in particular mercuric oxide, sulfate and dichloride, a Mettler Thermogravimetric Analyzer has proven to be very useful.

Results

Figure 1 illustrates the Raman spectrum of the yellowish colored deposit obtained in the very first experiment on this system. It was collected 6 ms downstream in the burned gases of an oxygen rich $C_3H_8/O_2/N_2$ (0.9/5/16) flame that contained 25 ppmv Hg, 75 ppmv SO_2, and 50 ppmv Cl_2 in the unburned gas flows. The probe was cooled to 60 ^oC with water. It was collected in two hours indicating a significant collection efficiency (30%) which compares almost exactly with similar deposits of alkali sulfates and carbonates. The deposit was a uniform smooth powder layer. As seen from Figure 1 and the comparison with the spectra of purchased samples, the deposit appears to be essentially quite pure mercuric sulfate. A second identical experiment, but without the sulfur dioxide, also yielded a deposit but this time it was brown in color.

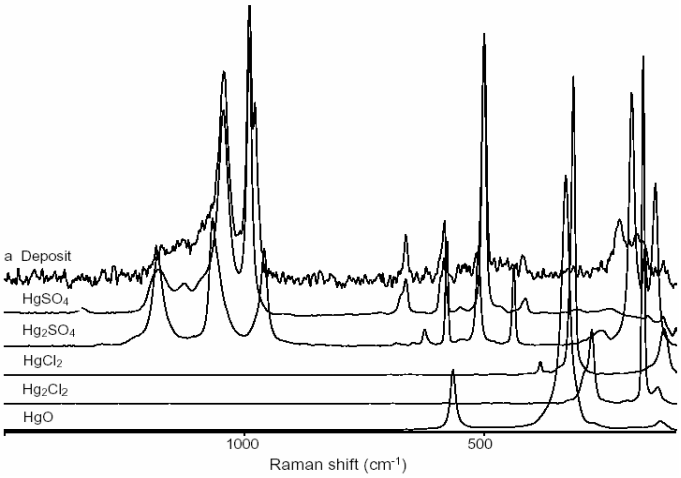

Figure 1. Raman spectrum of a flame generated deposit (a), compared to those of several purchased samples of pure anhydrous mercury compounds.

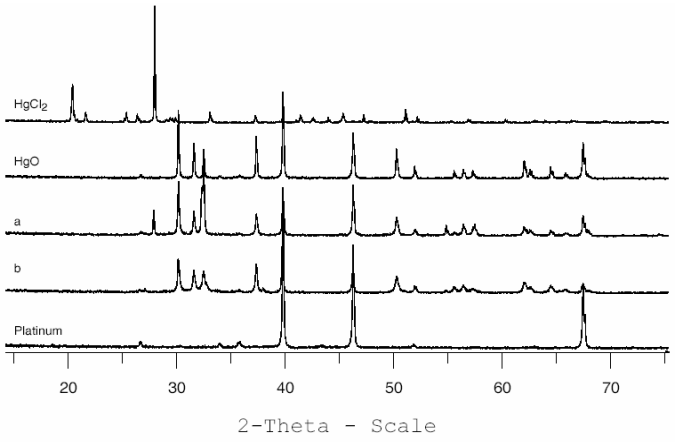

Figure 2. X-ray powder spectra of two flame deposits, (a) from a flame containing traces of mercury and chlorine, (b) from a similar flame but with no chlorine addition. These are compared to the spectra of purchased mercury compounds.

Its x-ray spectrum is indicated as trace a) in Fig. 2. A third experiment adding solely mercury to the flame gave a slightly larger also brown deposit. Its spectrum is trace b) in Fig. 2. Comparisons with other spectra clearly indicated that these deposits were mercuric oxide. However, trace a) also indicates the presence of a small contribution from mercuric dichloride. The lines of platinum present in these spectra result from scattering from the platinum strip substrate on which the samples are placed. These analyses were sufficient to indicate the heterogeneous chemistry of mercury and explain the formation mechanism of mercuric dichloride.

Consequently, as now confirmed by more than a hundred additional experiments, what happens in the exhaust gases is not as complicated as previously thought. The mercury on approaching the surface is rapidly converted to a molecular form. If sulfur is present then mercuric sulfate is produced. This is thermally stable up to about 550 ^{o}C. If the system is sulfur-free the mercury falls back to its second preference which is to form mercuric oxide. This is thermally stable to about 450 ^{o}C. Classical inorganic textbooks indicate that both of these can be vigorously attacked at temperatures above about 100 ^{o}C by chlorine and converted to mercuric dichloride. Serendipitously, solid mercuric dichloride is very volatile. It is labeled as a corrosive sublimate. Its vapor pressure is 10 torr at 180 ^{o}C, 50 at 230 ^{o}C, boiling at about 300 ^{o}C. As a result the mechanism is simple and elegant. Mercury deposits on any surface that the gases encounter, including ash particles, that have cooled sufficiently to permit the formation of the sulfate or oxide. This is then attacked in fact by hydrogen chloride that is the dominant chlorine source in burned gases. The deposit is converted to the dichloride, subliming back into the gas phase. The surface acts solely as a catalytic intermediate to facilitate the thermodynamic driving force for the formation of the very stable gaseous dichloride.

An examination of the condensed phase chemistry of molecular mercury indicates its rather limited extent. It does display two valences but consists mainly of its oxide, sulfate and halides. The carbonate, nitrates and sulfide are rather unstable and the hydride and hydroxide are not known. The results obtained herein display a preference for divalency and for sulfate over oxide. At higher temperatures there is an indication that the sulfate deposit becomes basic forming to some degree Schuetteite, $HgSO_4.2HgO$.

Deposits are obtained only under fuel lean conditions. Their rate of formation is first order in the mercury concentration and mercury is the dominant controlling species. This is evident in that sulfate and oxide deposition rates are the same. Deposition rates also are not sensitive to sulfur concentrations but do strongly depend upon the concentrations of chlorine in the flame gases. There is no evidence to support that the dichloride forms directly on the surface.

Experiments in cooler downstream locations (0.1s, 200 ^{o}C exhaust gas temperatures) have indicated, so far, a narrower formation temperature window than would be expected from the thermal stabilities of the sulfate and oxide. The lower formation threshold is about 150 ^{o}C, but the upper limit is only about 300 ^{o}C. This is being studied further but seems to result from competing reducing reactions that possibly arise from remaining trace levels of CO and/or H_2 in the exhaust gases from fuel lean combustion.

A New Emissions Mitigation Approach [6]

With this level of understanding of the emissions chemistry of mercury it now has been possible to develop a new method for its control. This is based on the concept of introducing a large surface area in the region of the cooling exhaust gases where the temperatures are optimal for mercury to deposit as the sulfate or oxide. The exhaust gases and hence mercury are made to encounter the surface numerous times during passage through this region. In this way an optimal conversion to dichloride can be achieved. The already present water scrubbers then can remove this.

Acknowledgement. This work made use of the MRL Central Facilities supported by the National Science Foundation under Award No. DMR00-80034.

References

(1) Niksa, S.; Fujiwara, N.; Fujita, Y.; Tomura, K.; Moritomi, H.; Tuji, T.; Takasu, S., *J Air &Waste Manage. Assoc.* **2002**, 52, 894- 901.
(2) Xu, M.; Qiao, Y.; Zheng, C.; Li, L.; Liu, J., *Combust Flame*, **2003**, 132, 208-218.
(3) Steinberg, M.; Schofield, K., *Twenty-Sixth Symposium (International) on Combustion,* The Combustion Institute, Pittsburgh, **1996**, 1835-1843.
(4) Schofield, K., *Combust. Flame*, **2003**,133, 147-156.
(5) Steinberg, M.; Schofield, K., *Combust. Flame*, **2002**, 129, 453-470.
(6) Schofield, K., U.S. Patent Application, May 1, 2003.

NICKEL SPECIATION OF URBAN PARTICULATE MATTER FROM DAVIE, FLORIDA

Kevin C. Galbreath,[1] Charlene R. Crocker,[1] Carolyn M. Nyberg,[1] Frank E. Huggins,[2] and Gerald P. Huffman[2]

[1]Energy & Environmental Research Center
University of North Dakota
15 North 23rd Street
Grand Forks, ND 58203

[2]CFFS/CME, University of Kentucky
105 Whalen Building
533 South Limestone Street
Lexington, KY 40506

Introduction

Nickel (Ni) from natural and anthropogenic sources pervades the environment. A significant natural source of atmospheric Ni is windborne dust particles derived from the weathering of rocks and soils and from volcanic eruptions.[1] Industrialization has increased its flux into the environment primarily through 1) combustion and incineration sources; 2) high-temperature metallurgical operations; 3) primary Ni production; and 4) chemical and catalyst manufacturing.[2, 3] The mobile source contribution to Ni emission inventories is small and derives primarily from engine wear and impurities in engine oil and fuel additives.[4] Commercial marine vessels are significant mobile sources of Ni in areas near harbors.[5]

Title III of the 1990 Clean Air Act Amendments (CAAA)[6] identifies 189 chemicals, including Ni, as potential hazardous air pollutants (HAPs). Many stationary sources have had to report Ni emissions as part of the U.S. Environmental Protection Agency's (EPA's) Toxics Release Inventory (TRI).[7] Although TRI and similar reporting provide estimates of the amounts of Ni released into the environment, they are not an indicator of toxicity because the acute, chronic, and cancer-causing effects vary significantly for the different chemical species of Ni. For example, nickel subsulfide (Ni_3S_2) is considered the most carcinogenic Ni species on the basis of available human epidemiology and animal studies.[3,8–10] The carcinogenicity of water-soluble Ni salts such as $NiSO_4 \cdot xH_2O$ and insoluble nickel oxide compounds such as Ni-containing spinels (e.g., $NiFe_2O_4$), however, is controversial.[3, 10, 11] Therefore, determining the speciation of Ni in ambient air is of the utmost importance for assessing the respiratory health risks associated with Ni.

Ni speciation analyses were conducted on urban total suspended particulate (TSP), PM_{10}, and $PM_{2.5}$ samples collected from Davie, Florida, using x-ray absorption fine structure (XAFS) spectroscopy. Automated scanning electron microscopy (ASEM) was also used to determine the number concentrations (frequency %) of Ni-containing particles in Davie, Florida, TSP and to evaluate the particle-size distributions of Ni.

Experimental

Ambient TSP, PM_{10}, and $PM_{2.5}$ samples were collected continuously during August 26–31, 2002, from an urban Broward County State and Local Air Monitoring Station (SLAMS) and National Air Monitoring System (NAMS) site located in Davie, Florida (26.08°N, 80.24°W). The locations of major PM_{10} point sources in relation to the sampling site and a wind rose diagram for the sampling period are shown in **Figure 1**. The PM_{10} emission estimates in **Figure 1** are based on 2001 statistics from the Florida Department of Environmental Protection. Point sources in the vicinity of the Davie site include residual (No. 6 fuel) oil- and gas-burning power plants, cement kiln operations, and municipal waste incineration facilities. Significant mobile sources of TSP, PM_{10}, and $PM_{2.5}$ near the Davie site include motor vehicle, aircraft, and marine vessel traffic. The wind rose diagram in **Figure 1**, created from hourly average wind speed and direction measurements from the Fort Lauderdale International Airport, indicates that winds were predominantly marine in origin and that mobile and point sources east-southeast and southeast of the Davie site probably contributed to TSP, PM_{10}, and $PM_{2.5}$ during the sampling period.

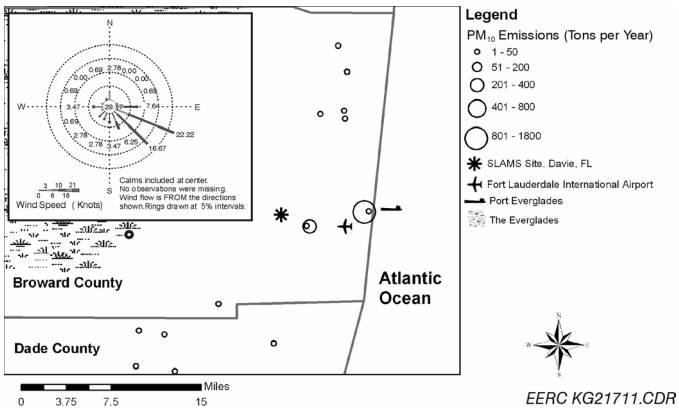

Figure 1. Davie, Florida, SLAMS/NAMS site, major PM_{10} point source, Fort Lauderdale International Airport, and Port Everglade locations and a wind rose diagram for the sampling period.

The following equipment and EPA Compendium Methods[12] were used to sample ambient TSP, PM_{10}, and $PM_{2.5}$:

- Tapered electronic oscillating microbalance (TEOM), Rupprecht & Patashnick Model 1400a (EPA Compendium Method IO-1.3).
- Automatic cartridge collection unit (ACCU), Rupprecht & Patashnick
- Sequential air sampler (SAS), Rupprecht & Patashnick Model 2025 (EPA Compendium Method IO-2.3)
- High-volume air sampler (HVAS), General Metal Works (EPA Compendium Method IO-2.1)

TSP was collected on Type A/E glass fiber filters, whereas PM_{10} and $PM_{2.5}$ were collected on GF/C glass fiber filters. Urban TSP was also collected on a moving carbon tape using a Burkard seven-day recording volumetric spore trap (BVST). Field filter blank samples were collected for quality control purposes. Ni concentrations of the field filter blanks, Davie TSP, and a National Institute for Standards and Technology (NIST) standard reference material (SRM) 1648 (urban TSP) were determined using microwave digestion followed by graphite furnace atomic absorption spectroscopy (GFAAS).

X-Ray Absorption Fine Structure Spectroscopy. Ni and S XAFS spectra were obtained at beam lines X-18B and X-19A, respectively, of the National Synchrotron Light Source (NSLS), Brookhaven National Laboratory, New York. Ni XAFS spectra were collected in fluorescence mode using a multielement Ge detector, whereas the S XAFS spectra were collected in the same mode using a Passivated Implanted Planar Silicon (PIPS) detector. Multiple scans, typically between three and five scans, were combined to produce the overall spectrum. Ni XAFS spectra were analyzed using the procedures described by Brown et al.,[13] Lee et al.,[14] and Koningsberger and Prins.[15] XANES spectra of reagent-grade Ni compounds and synthesized Ni compounds, acquired in previous

investigations,[16–18] were used essentially as "fingerprints" for identifying and quantifying Ni species. The following Ni compounds are included in this spectral database: Ni^0, NiS, NiS_2, Ni_3S_2–Ni_7S_6 mixture, NiO, $Ni(OH)_2$, $NiSO_4 \cdot xH_2O$, $C_4H_6NiO_4 \cdot 4H_2O$, $NiCO_3$, and $NiFe_2O_4$.

Automated Scanning Electron Microscopy. The ASEM method utilizes digital image analysis and electron probe microanalysis (EPMA) techniques to locate, size, and chemically analyze individual ash particles with submicron diameters as small as 0.3 μm. Particles collected on the carbon tape of the BVST were analyzed for Ni using the ZAF method which corrects x-ray intensities for differences in the atomic number (Z), absorption (A), and fluorescent (F) effects of the calibration standards relative to the sample. The chemical composition obtained in this manner is semiquantitative at best because of the short x-ray counting time employed (10 s), the use of flat mineral standards for calibration, and the fact that no matrix corrections for particle diameter, shape, or density were applied.

Results and Discussion

Sulfur K-Edge XAFS Spectroscopy Analyses. The absorption intensities for the TSP-, PM_{10}-, and $PM_{2.5}$-containing filters are significantly greater than the absorption signals for the corresponding blank filters. Hence, the sulfur absorptions are primarily caused by the PM_{10} and $PM_{2.5}$ trapped within the filters. The energy location of the sulfur peaks in sulfur XANES spectra for the SAS filter blank and the filters containing TSP, PM_{10}, and $PM_{2.5}$ are all consistent with the presence of the sulfate (SO_4) species. The XANES sulfur species detection limit is approximately 3% of the total sulfur present, thus >95% of the sulfur in Davie TSP, PM_{10}, $PM_{2.5}$, and SAS filter blank is present as SO_4-based compounds.

Nickel K-Edge XAFS Spectroscopy Analyses. Ni K-edge XAFS spectra for filter blanks and filters containing Davie TSP, PM_{10}, and $PM_{2.5}$ indicated that Ni is mostly concentrated in PM_{10}. Duplicate GFAAS analyses of Davie TSP indicated that it contains 86 ppm Ni. Ni absorption is approximately proportional to Ni concentration; thus the Davie PM_{10} sample was estimated to contain approximately 140 ppm Ni. These Davie TSP and PM_{10} Ni concentrations correspond to airborne Ni concentrations of ≈1.5 ng/m^3, which is very similar to the annual average ambient Ni concentration of 1.9 ng/m^3 estimated for Broward County by EPA.[19] These Ni concentrations are much lower in comparison to average urban ambient air Ni concentrations, which range from 5 to 50 ng/m^3 and are more representative of Ni concentrations found in remote and rural areas.[8, 9, 20, 21] The low airborne Ni concentrations at the Davie, Florida, air-monitoring site may represent the atmospheric burden of "background" Ni derived from long-range transport via the southeast and easterly North Atlantic trade winds (**Figure 1**).

The Ni K-edge absorption signals from the filters containing Davie TSP and PM_{10} were sufficiently intense to process and create XANES spectra. Spectra from the Ni XANES database were compared to the TSP and PM_{10} spectra using a least squares fitting procedure. Estimates, based on the least squares fitting, of the Ni species compositions of Davie TSP and PM_{10} are provided in **Table 1**. Davie PM_{10} contains a much greater proportion of $NiSO_4 \cdot xH_2O$ relative to TSP, probably because of the greater surface area of PM_{10} on which $NiSO_4 \cdot xH_2O$ heterogeneously condensed or adsorbed.

Table 1 XANES Ni Speciation Results for Davie TSP and PM_{10}, % of Total Ni

Ni Species	TSP	PM_{10}
$NiSO_4 \cdot xH_2O$	40	78
$NiFe_2O_4$	50	22
NiS	10	<5

ASEM. Approximately 800 to 1100 urban TSP particles were analyzed at random on portions of the BVST carbon tape using ASEM. Compared in **Figure 2** are the number concentrations of Ni-bearing particles, arbitrarily defined as containing ≥10 wt% Ni, sampled during each of four days (August 27–30, 2002). Approximately 8% of the particles sampled on August 27, 29, and 30 contained ≥10 wt% Ni, whereas on August 28 about 15% of the particles were Ni-bearing. Apparently, additional emission sources of Ni were contributing to the TSP sample collected on August 28 or the Ni emission rate for a particular source in the Davie, Florida, area increased on August 28.

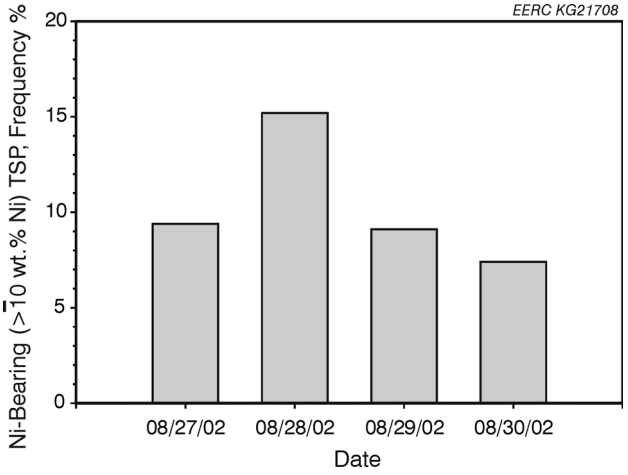

Figure 2. Number concentrations of Ni-bearing (≥10 wt %) particles in Davie TSP samples.

The particle-size distributions of Ni-bearing particles are compared in **Figure 3**. Most of the Ni-bearing particles are <10 μm in diameter, indicating that they were released from combustion sources. Ni-bearing particles sampled on August 30 were significantly coarser relative to those sampled on August 27–29.

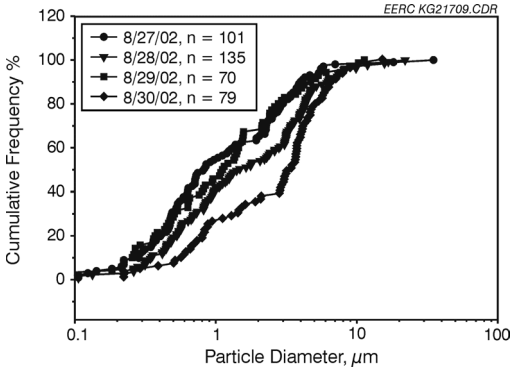

Figure 3. Particle-size distribution of Ni-bearing (≥10 wt%) particles in Davie TSP.

Conclusions

The airborne Ni concentration of .1.5 ng/m^3 measured at the Davie, Florida, SLAMS/NAMS site during August 26–31, 2002, is similar to the EPA estimated annual average ambient Ni concentration of 1.9 ng/m^3 for Broward County.[19] Approximately 8%–15% of the total number of particles sampled from the Davie, Florida, SLAMS/NAMS site contained significant Ni concentrations, ≥10 wt%. Most of these Ni-bearing particles were <10 μm in diameter. XANES results indicated that $NiSO_4 \cdot xH_2O$ and a nickel oxide compound, possibly $NiFe_rO_4$, were the dominant Ni species occurring in TSP, although a small proportion of NiS was also present. The PM_{10} fraction lacked NiS, but $NiSO_4 \cdot xH_2O$ was much more abundant in comparison to TSP, probably because of the greater surface area of PM_{10} on which $NiSO_4 \cdot xH_2O$ heterogeneously condensed or adsorbed. The quantity of the $PM_{2.5}$ fraction was insufficient to quantify Ni and perform speciation analyses. Sulfur K-edge XANES analyses indicated that >95% of the total sulfur in the TSP, PM_{10}, and $PM_{2.5}$ samples is present as SO_4.

Acknowledgment. This investigation was supported by the Nickel Producers Environmental Research Association (NiPERA) through the Energy & Environmental Research Center (EERC) Jointly Sponsored Research Program, which is supported by the U.S. Department of Energy (DOE) National Energy Technology Laboratory under Cooperative Agreement No. DE-FC26-98FT40321. We are grateful to Mr. Kenneth P. Larson of the Broward County Commission, Department of Planning and Environmental Protection, Air Quality Division, for facilitating the EERC sampling of urban particulate matter at its SLAMS/NAMS site in Davie, Florida. XAFS investigation of fossil fuel-derived particulate matter is supported in part by a National Science Foundation Collaborative Research Activities in Environmental Molecular Science grant to the University of Kentucky. We also acknowledge DOE for its support of synchrotron facilities, without which this work would have been impossible.

References

1. Nriagu, J.O. A Global Assessment of Natural Sources of Atmospheric Trace Metals, *Nature* **1989**, *338*, 47–49.
2. U.S. Environmental Protection Agency. *Locating and Estimating Air Emissions from Sources of Nickel*; Office of Air Quality Planning and Standards, Research Triangle Park, NC, March 1984, EPA-450/4-84-007f.
3. Nickel Producers Environmental Research Association (NiPERA). *Occupational Exposure Limits Criteria Document for Nickel and Nickel Compounds, Volume 1: Summary, Conclusions, and Recommendations;* Prepared for the European Commission, Directorate-General V, Public Health and Safety at Work Directorate. Prepared by NiPERA in collaboration with Eurometaux, Dec 24, 1996.
4. U.S. Environmental Protection Agency. *Documentation for the 1996 Base Year National Toxics Inventory for Onroad Sources*; Emission Factor and Inventory Group (MD-14); Emissions, Monitoring and Analysis Division, Research Triangle Park, NC, June 2000.
5. U.S. Environmental Protection Agency. *Documentation for Aircraft, Commercial Marine Vessel, Locomotive, and Other Nonroad Components of the National Emissions Inventory*; Emission Factor and Inventory Group (D205-01); Emissions, Monitoring and Analysis Division, Research Triangle Park, NC, Nov 2002.
6. *Provisions for Attainment and Maintenance of National Ambient Air Quality Standards*; U.S. Public Law, 101–549, 1990.
7. U.S. Environmental Protection Agency. *1996 Toxics Release Inventory, Public Data Release–Ten Years of Right-to-Know*; EPA 745-R-08-005, Washington, DC, May 1998.
8. Agency for Toxic Substances and Disease Registry (ATSDR). *Toxicology Profile for Nickel*; Prepared by Sciences International, Inc., under subcontract to Research Triangle Institute under Contract No. 205-93-0606, U.S. Department of Health and Human Services, Public Health Service, Atlanta, GA, Sept 1997.
9. Health Canada, Canadian Environmental Protection Act. *Priority Substances List: Supporting Documentation, Health-Related Sections, Nickel and Its Compounds*; Ottawa, Canada, 1993.
10. U.S. Environmental Protection Agency. *Study of Hazardous Air Pollutant Emissions from Electric Utility Steam Generating Units—Final Report to Congress: Volume 1*; EPA–453/R–98–004a, Washington, DC, Feb 1998.
11. Toxicology Excellence for Risk Assessment (TERA). *Toxicological Review of Soluble Nickel Salts;* Prepared for the Metal Finishing Association of Southern California, Inc., U.S. Environmental Protection Agency, and Health Canada. Prepared by TERA under subcontract in part with Science Applications International Corporation, EPA Contract No. 68-C7-0011, March 1999.
12. U.S. Environmental Protection Agency. *Compendium of Methods for the Determination of Inorganic Compounds in Ambient Air*; EPA/625/R-96/010a, Washington, DC, June 1999.
13. Brown, G.E., Jr.; Calas, G. ; Waychunas, G.A.; Petiau, J. In Hawthorne, F.C., Ed.; *Spectroscopic Methods in Mineralogy and Geology*; Rev. in Mineral. Vol. 18, Mineralogical Society of America, Washington, DC, 1988, Chapter 11, pp 431–512.
14. Lee, P.A.; Citrin, P.H.; Eisenberger, P.; Kincaid, B.M. *Rev. Mod. Phys*. **1981**, *53*, 769–808.
15. Koningsberger, D.C.; Prins, R. *X-Ray Absorption. Principles, Applications, Techniques of EXAFS, SEXAFS, and XANES*, J. Wiley & Sons: New York, 1988.
16. Galbreath, K.C.; Zygarlicke, C.J.; Toman, D.L.; Huggins, F.E.; Huffman, G.P. Nickel and Chromium Speciation of Residual Oil Combustion Ash, *Combust. Sci. Technol.* **1998**, *134* (1–6), 243–262.
17. Galbreath, K.C.; Zygarlicke, C.J.; Huggins, F.E.; Huffman, G.P.; Wong, J. Chemical Speciation of Nickel in Residual Oil Ash. *Energy Fuels* **1998**, *12*, 818–822.
18. Galbreath, K.C.; Toman, D.L.; Zygarlicke, C.J.; Huggins, F.E.; Huffman, G.P.; Wong, J. Nickel Speciation of Residual Oil Fly Ash and Ambient Particulate Matter Using X-Ray Absorption Spectroscopy. *J. Air Waste Manage. Assoc.* **2000**, *50 (11)*, 1876–1886.
19. U.S. Environmental Protection Agency. *National Air Toxics Assessment*, 1996, http://www.epa.gov/ttn/atw/nata/tablconc.html (accessed April 16, 2003).
20. Schroeder, W.H.; Dobson, M.; Kane, D.M. Toxic Trace Elements Associated with Airborne Particulate Matter: A Review, *Air Pollut. Control Assoc.* **1987**, *11*, 1267–1287.
21. Sunderman, Jr., F.W.; Oskarsson, A. *Nickel,* In *Metals and Their Compounds in the Environment: Occurrence, Analysis, and Biological Relevance*, Merian, E., Ed.; VCH: Weinheim, 1991, pp 1101–1126.